THE NRAO VLA SKY SURVEY

J. J. Condon, W. D. Cotton, E. W. Greisen, and Q. F. Yin
National Radio Astronomy Observatory[1], 520 Edgemont Road, Charlottesville, VA 22903
Electronic mail: [jcondon,bcotton,egreisen,qyin]@nrao.edu

R. A. Perley and G. B. Taylor
National Radio Astronomy Observatory[1], P. O. Box 0, Socorro, NM 87801
Electronic mail: [rperley,gtaylor]@nrao.edu

J. J. Broderick
Physics Department, Virginia Polytechnic Institute and State University, Blacksburg, VA 24061
Electronic mail: jjb@vt.edu

ABSTRACT

The NRAO VLA Sky Survey (NVSS) covers the sky north of J2000 $\delta = -40°$ (82% of the celestial sphere) at 1.4 GHz. The principal data products are (1) a set of 2326 $4° \times 4°$ continuum "cubes" with three planes containing Stokes I, Q, and U images plus (2) a catalog of almost 2×10^6 discrete sources stronger than $S \approx 2.5$ mJy. The images all have $\theta = 45''$ FWHM resolution and nearly uniform sensitivity. Their rms brightness fluctuations are $\sigma \approx 0.45$ mJy beam$^{-1} \approx 0.14$ K (Stokes I) and $\sigma \approx 0.29$ mJy beam$^{-1} \approx 0.09$ K (Stokes Q and U). The rms uncertainties in right ascension and declination vary from $\lesssim 1''$ for the $N \approx 4 \times 10^5$ sources stronger than 15 mJy to $7''$ at the survey limit.

The NVSS was made as a service to the astronomical community. All data products, user software, and updates are being released via the World Wide Web as soon as they are produced and verified.

Subject headings: catalogs — methods: data analysis — methods: observational — radio continuum — surveys

[1]The National Radio Astronomy Observatory is a facility of the National Science Foundation operated under cooperative agreement by Associated Universities, Inc.

1. Introduction

We used the compact D and DnC configurations of the Very Large Array (VLA) between 1993 September and 1996 October to make 1.4 GHz continuum total-intensity and linear-polarization images covering the $\Omega \approx 10.3$ sr of sky with J2000 $\delta \geq -40°$. Additional observations were made during the fourth quarter of 1997 to fill small gaps in this coverage. The full NRAO VLA Sky Survey (NVSS) is based on 217,446 "snapshot" observations of partially overlapping primary-beam areas, each of which was imaged separately. The small snapshot images were weighted, corrected, and combined to yield a set of 2326 large ($4° \times 4°$) image "cubes" whose third axes span the Stokes polarization parameters I, Q, and U. All NVSS images have a circular Gaussian point-source response whose full-width between half-maximum (FWHM) points is $\theta = 45''$, significantly larger than the median angular size ($\phi \approx 10''$) of faint extragalactic sources, in order to achieve the high surface-brightness sensitivity needed for flux-limited completeness and good photometric accuracy. The large images have rms brightness fluctuations $\sigma \approx 0.45$ mJy beam^{-1} ≈ 0.14 K rms in total intensity and $\sigma \approx 0.29$ mJy beam^{-1} ≈ 0.09 K in Stokes Q and U. The catalog of sources extracted from these images contains nearly 2×10^6 objects, including radio galaxies and quasars, most of the galaxies in the *IRAS* Faint Source Catalog (Moshir *et al.* 1992), ultraluminous starburst galaxies even at cosmological distances, plus statistically useful numbers ($N \gg \sqrt{N}$) of nearby "normal" galaxies, low-luminosity active galactic nuclei (AGN), galactic planetary nebulae, pulsars, and stars. Although the NVSS observing frequency was determined primarily by technical considerations, 1.4 GHz lies in the "intermediate-frequency gap" between higher frequencies associated with significant intrinsic source variability and lower frequencies at which there is strong variability caused by refractive interstellar scintillations (Spangler & Cotton 1981). Consequently, the NVSS images should accurately reflect the radio sky for decades to come.

All NVSS results are available to the entire astronomical community. The survey team reserves no proprietary rights to either the raw data or the final data products because we believe that the scientific potential of large surveys can be realized only if all astronomers have full and immediate access to them. To encourage use of the NVSS, we have adopted the following policies for NVSS results: (1) Any astronomer may access the uncalibrated VLA "archive" data immediately, without waiting for the usual one year proprietary-data period to end. (2) Our calibrated (u, v) data and uncorrected snapshot images are likewise available for copying at any time. (3) The principal data products of interest to most users—the corrected $4° \times 4°$ images, the catalog of sources found on them, plus software for their use and any updates—are being released via the World Wide Web (Condon *et al.* 1998) as soon as they are made and verified. The NVSS team members have agreed to use only these electronically released results for their own research.

This paper reviews the known properties of faint radio-source populations and explains how they influenced the NVSS design and scientific goals. It introduces a number of new techniques that were used for the NVSS observations, calibration, imaging, and source fitting. It also describes the error analysis and verification tests of the NVSS data products. Conscientious users who want to skip the details should at least read the user summary (Section 5.3) and recognize those limitations of the NVSS which are not well represented by simple Gaussian error distributions. *Caveat emptor.*

2. Scientific Goals and Survey Design

Both very deep ($S \ll 1$ mJy) and large-scale ($\Omega \gg 1$ sr) radio surveys already exist at 1.4 GHz, so we can use the known features of the relevant source populations to optimize the design of a moderately deep large-scale radio survey. Nearly all discrete radio sources more than a one or two degrees from the Galactic plane are extragalactic. The weighted differential counts of extragalactic sources found at $\nu = 1.4$ GHz are shown in Figure 1.

There are two astrophysically distinct populations of extragalactic radio sources: (1) Over 99% of the stronger ($S \gtrsim 60$ mJy at 1.4 GHz) sources found in earlier large-scale surveys are classical radio galaxies and quasars powered by "monsters" (e.g., supermassive black holes) in AGN. (2) An increasing fraction of fainter sources can be identified with low-luminosity AGN and star-forming galaxies containing H II regions ionized by massive ($M \gtrsim 8 M_\odot$) short-lived ($\tau \lesssim 3 \times 10^7$ yr) stars and relativistic electrons accelerated by their supernova remnants (Condon 1992). These star-forming galaxies are not usually considered to be "true" AGN, although ultraluminous ($L > 2 \times 10^{11} L_\odot$ if $H_0 = 75$ km s^{-1} Mpc^{-1}) nuclear "starbursts" are often quite compact ($r \sim 100$ pc) and similar in many other observables to AGN powered by monsters (Sanders *et al.* 1988, Condon *et al.* 1991c). The majority of radio sources powered by stars lie in ordinary spiral galaxies. Their median face-on disk brightness temperature is just $\langle T \rangle \approx 1$ K at $\nu = 1.4$ GHz, so they can be detected only by a relatively low-resolution survey, regardless of their distance. For example, $T = 1$ K corresponds to a peak flux density $S_{\rm P} \approx 3$ mJy beam^{-1} in the $\theta = 45''$ FWHM Gaussian synthesized beam of the VLA D configuration but just $S_{\rm P} \approx 0.3$ mJy beam^{-1} for the $\theta = 15''$ resolution of the C configuration. Reaching the same brightness sensitivity with the C configuration would require a factor of 10^2 increase in integration time.

Radio sources in star-forming galaxies generally obey the tight far-infrared (FIR) to radio luminosity correlation (Condon *et al.* 1991a and references therein). Consequently, flux-limited samples of such galaxies selected in the radio and FIR bands are nearly identical. The median FIR/radio luminosity ratio for a $\lambda = 60\mu$m sample is $\langle \log(S_{60\mu{\rm m}}/S_{1.4{\rm GHz}}) \rangle \approx 2.15$ (Condon & Broderick 1986), so the NVSS should detect the majority of galaxies above the *IRAS* Faint Source Catalog, Version 2 (Moshir *et al.* 1992) $S_{60\mu{\rm m}} = 0.28$ Jy completeness limit. The cumulative fractions $f(<z)$ of star-forming galaxies with redshifts $< z$ are plotted for three different 1.4 GHz flux-density levels in Figure 2. The stronger starburst sources are local ($z \ll 1$), but deep radio surveys can detect luminous starbursts even at cosmological distances. Evolution is negligible above 100 mJy, detectable at 10 mJy, and quite significant below 1 mJy. The combination of the *IRAS* FSC2 and the NVSS may reveal new and exotic objects similar to the ultraluminous object FSC10214+4724 at $z \approx 2.3$ (Rowan-Robinson *et al.* 1991) because the NVSS can provide more accurate positions for making unambiguous optical identifications of distant, luminous starbursts in optically faint galaxies. Many ultraluminous starbursts are so compact that they are transparent *only* in the radio and FIR bands (Condon *et al.* 1991c), so radio or FIR observations are essential for quantitative studies of these objects.

Even the fairly sensitive Green Bank sky survey detected only ~ 30 "starburst" sources sr^{-1} among the 10^4 sr^{-1} sources stronger than 25 mJy at 4.85 GHz (equivalent to about 60 mJy at 1.4 GHz). At this level, only 1 in 300 extragalactic radio sources is powered by stars—such sources are almost as rare as gravitational lenses. There are just enough examples known for the simplest statistical tests. For example, Cox *et al.* (1988) showed that the FIR/radio correlation is nonlinear using a sample of spiral galaxies brighter than $m \sim 14.5$ detected in the 6C 151 MHz surveys. The NVSS should multiply the number of known radio sources in this star-forming population by 10^2.

Classical radio sources powered by AGN are typically two orders of magnitude rarer (per unit volume) and more luminous than those in star-forming galaxies. Cosmological evolution dominates their redshift distribution even at high flux densities. Figure 3 shows that their median redshift is $\langle z \rangle \sim 0.8$ with surprisingly little dependence on flux density below $S \sim 1$ Jy and that very few are nearby ($z \ll 1$). Consequently, making complete and reliable optical identifications, spectroscopic observations, and other follow-up studies of distant radio AGN is difficult even in tiny ($\Omega \ll 1$ sr) areas (cf. Windhorst *et al.* 1990). The scarcity of nearby radio AGN means that there is very little overlap between flux-limited samples of AGN selected in radio and other (e.g., FIR, optical, or X-ray) bands. For example, only one in 200 AGN stronger than 25 mJy at 4.85 GHz is close enough ($D \lesssim 100$ Mpc) to appear in the UGC Catalog (Nilson 1973) of galaxies with optical angular diameters $\geq 1'$ (Condon *et al.* 1991b). The rare nearby radio galaxies are scientifically valuable because they can be studied in greater detail—their optical morphologies can be determined, their optical spectra and redshifts are easy to obtain, a given angular resolution yields better linear resolution, etc. For the first time, the NVSS should detect thousands of the nearest AGN over most of the sky.

These radio source characteristics imply conflicting requirements for survey resolution—we need low resolution to detect low-brightness sources and to measure accurate flux densities of extended sources, but we want high resolution to determine accurate radio positions and identify faint radio sources with galaxies at high redshifts. The following argument shows why no single survey can do both well.

The intensity displayed on a radio image has dimensions of brightness (units such as mJy beam^{-1} or K), not flux density (mJy). Survey images and source catalogs derived from them are therefore *brightness* sensitivity limited. Most scientific applications of surveys require samples limited by source flux density, not image brightness, a quantity dependent on instrumental resolution. Beware that the common but misleading term "peak flux density" actually refers to image brightness. The desired uniformly low flux-density limit can be attained only by those surveys which do not resolve most faint sources. For example, a survey complete to a peak flux density of 1 mJy beam^{-1} will miss those sources weaker than 2 mJy which are extended over two or more beam solid angles. This distinction between brightness and flux density was safely ignored in earlier large-scale surveys made with single-dish telescopes or with interferometers operating at such long wavelengths that nearly all extragalactic sources were unresolved, but the larger VLA configurations do resolve them. A simple approximation to the cumulative angular-size distribution of faint sources selected near 1.4 GHz (Windhorst *et al.* 1990) is shown in Figure 4. The $\theta = 45''$ resolution of the *smallest* VLA configuration is actually the *highest* resolution consistent with high survey completeness, both for distant AGN and for nearby spiral galaxies. We consider completeness to be the most fundamental requirement of a survey because follow-up observations can always increase the resolution on a detected source, but a missed source is lost forever.

Uniformly accurate flux densities are also important for nearly all scientific applications of survey images. The poor (u, v)-plane coverage of a single VLA snapshot makes it difficult to obtain good photometic accuracy on source components extended by more than a few synthesized beamwidths. In addition, the noise error on the flux density of a faint source is multiplied by the square root of the number of independent beam areas covered by the source. Thus Figure 4 also favors $\theta \gtrsim 45''$ for uniformly high photometric accuracy.

Radio spectra are best determined from flux densities measured with nearly the same beam size at all frequencies, particularly if the sources are resolved. The 151 MHz 7C survey (McGilchrist *et al.* 1990) with $70'' \times 70'' \sec\delta$ resolution, the 327 MHz Westerbork Northern Sky Survey (WENSS) that will cover the sky north of $\delta = +30°$ with $55'' \times 55'' \sec\delta$ resolution and a 15 mJy detection limit (de Bruyn *et al.* 1994, Rengelink *et al.* 1997) , and the Molonglo 408 MHz survey (Green 1997) that will eventually map $\delta < -30°$ with $43'' \times 43'' \sec\delta$ resolution are all well matched to the $45''$ resolution of D-configuration VLA images for spectral work (e.g., selecting high-redshift galaxies by their steep radio spectra).

Confusion by blends of faint extragalactic sources ultimately limits the possible sensitivity of surveys made with any given resolution. The rms confusion has been measured at 1.49 GHz; it is $\sigma_c \approx 0.011$ mJy in a $\theta = 17\overset{''}{.}5$ FWHM Gaussian beam (Mitchell & Condon 1985). The differential number $n(S)dS$ of sources per steradian with flux densities between S and $S + dS$ is approximately a power law with slope -2 in the flux-density range $0.01 \lesssim S \lesssim 1$ mJy, so the rms confusion brightness temperature is ≈ 0.02 K at 1.49 GHz, nearly independent of resolution in the range $5'' \lesssim \theta \lesssim 3'$ (Condon 1974). In this range, the confusion flux density scales as $\sigma_c \propto \theta^2 \nu^{-\langle\alpha\rangle}$, where $\langle\alpha\rangle \approx +0.7$ is the median spectral index. The rms confusion from faint extragalactic sources in a $\theta = 45''$ Gaussian beam should be only $\sigma_c \approx 0.08$ mJy, which is well below the receiver noise level for VLA snapshots with integration times < 5 minutes. Sidelobes of the dirty beam from a VLA snapshot cannot be cleaned completely, so the confusion fluctuations in NVSS images are somewhat larger than this. The resolution needed to avoid the confusion limit approaches but does not yet conflict with the need for a beam larger than most faint sources.

Radio sources can be identified by position coincidence with sources detected in other wavebands. Noise limits the rms position uncertainty $\sigma_{\rm p}$ in each fitted sky coordinate (α or δ) of a faint point source found on an image having rms brightness fluctuation σ and FWHM resolution θ to (Ball 1975, Condon 1997)

$$\sigma_{\rm p} \approx \left(\frac{\sigma\theta}{2S_{\rm P}}\right) , \tag{1}$$

where $S_{\rm P}$ is the peak flux density of the source in the image. Near the detection limit ($S_{\rm P} \approx 5\sigma$) of any survey, the rms position uncertainty contributed by noise alone approaches $\sigma_{\rm p} \approx \theta/10$. The largest position uncertainties for a snapshot VLA survey are somewhat larger ($\lesssim 7''$, Equation 25) because the poor (u, v)-plane coverage causes the noise correlation length to be larger than θ. This accuracy is still sufficient for identifications with most sources found in other wavebands, where the source densities are low and the uncertainties of the positions are often larger. However, significantly higher resolution is needed to identify the weakest detectable radio sources with optically faint galaxies.

The position accuracy required to achieve a given identification completeness C ($0 \leq C \leq 1$) and reliability R ($0 \leq R \leq 1$) depends on the sky density ρ_* of indentification candidates, the identification search radius $r_{\rm s}$, and the *a priori* probability f that an identification exists (Condon *et al.* 1975):

$$C = [1 - \exp(-km^2/2)]/k \tag{2}$$

$$R = C/\{f^{-1} + (1 - f^{-1})\exp[m^2(1-k)/2] - \exp(-m^2k/2)\} , \tag{3}$$

where $k \equiv 1 + 2\pi\rho_*\sigma_{\rm p}^2$ and $m \equiv r_{\rm s}/\sigma_{\rm p}$. The most severe requirements are for unrestricted position-coincidence optical identifications because the density $\rho_* = \rho_{\rm g} + \rho_{\rm q} + \rho_{\rm s}$ of all faint galaxies, quasars, and foreground stars is very high. At the UK Schmidt and POSS II limit $J \approx 22.5$, $\rho_{\rm g} \approx 1.7 \times 10^3$ deg^{-2} (Peterson *et al.* 1979) and $\rho_{\rm q} \approx 160$ deg^{-2} (Hartwick & Schade 1990). The sky density of stars varies from $\rho_{\rm s} \approx 2 \times 10^3$ deg^{-2} near the galactic pole to $\rho_{\rm s} \approx 4 \times 10^3$ deg^{-2} at $|b| \approx 30°$, $|l| \approx 90°$ and reaches $\rho_{\rm s} \approx 10^4$ deg^{-2} in the bulge ($|b| \lesssim 30°$, $|l| \lesssim 45°$) (Bahcall & Soneira 1980, 1981). About 30% of all mJy-level radio sources selected at 1.4 GHz can be identified with galaxies or quasars brighter than $J \approx 22.5$ (Windhorst *et al.* 1984), so $f \approx 0.3$. If the normalized search radius m is chosen to make $C \approx R$, then completeness and reliability decrease with increasing rms position uncertainty as shown in Figure 5. Both begin to fall rapidly as the rms position uncertainty exceeds $\sigma_{\rm p} \approx 3''$, depending on the galactic foreground. Thus surveys made with beams smaller than $20 - 30''$ are necessary if the faintest detectable radio sources are to be identified with the faintest objects in these or deeper optical sky surveys. The $\theta = 5\farcs4$-resolution B-configuration FIRST survey (Becker *et al.* 1995) is the best example; it is complete to ≈ 1 mJy beam^{-1} in a large area centered on the north galactic cap.

Most of the $N \approx 10^6$ NVSS sources stronger than 5 mJy have $\sigma_{\rm p} \lesssim 3''$ and can be identified with $\gtrsim 90\%$ completeness and reliability except near the galactic bulge, where $C \approx R \gtrsim 80\%$. Above 15 mJy, $\sigma_{\rm p} \lesssim 1''$ and the NVSS identifications of these $N \approx 4 \times 10^5$ sources should be quite complete and reliable everywhere. The faintest NVSS sources have $\sigma_{\rm p} \lesssim 7''$. If the search radii suggested by Figure 5 are used, these sources can be optically identified by position coincidence with any objects on the UK Schmidt or POSS II IIIa-J plates with only 70% completeness and reliability at high Galactic latitudes about 45% completeness and reliability in crowded fields near the galactic bulge. Optically faint identifications of the weakest NVSS sources should therefore be verified by directed observations made with higher resolution.

Radio survey catalogs are frequently used to determine whether a particular astronomical object is a radio source. The required position accuracy depends primarily on the density of sources in the radio catalog. For example, the NVSS catalog contains $\rho \approx 50$ sources per square degree. The probability that the nearest unrelated NVSS source lies within angular distance r of any position is

$$P(< r) = 1 - \exp(-\pi \rho r^2) \ , \tag{4}$$

as illustrated by Figure 6. The probability of a "false alarm" is only about 0.01 for $r < 30''$, so rms position uncertainties smaller than about $10''$ are sufficient for this purpose.

By far the greatest cost of major surveys such as the NVSS is telescope time. One way to measure efficient use of this time is the rate at which sources are found. For any total observing time T, there is a tradeoff between the solid angle Ω surveyed and the integration time τ spent on each position: $T \propto \Omega\tau$. Above the confusion limit, increasing τ decreases the detection limit roughly as $S \propto \tau^{-1/2}$. If the cumulative density of sources is $N(> S) \propto S^{-\beta}$, the rate of source detection is proportional to $\tau^{(\beta-2)/2}$. The actual source count is not a power law, but Figure 7 shows how the effective β varies with flux density at $\nu = 1.4$ GHz. At high flux densities ($S \approx 1$ Jy), β is nearly two, and the rate of source detection is almost independent of the integration time chosen. Near $S = 2$ mJy the slope has a minimum $\beta \approx 0.7$ and the detection rate is proportional to $\tau^{-0.65}$, strongly favoring short integrations and wide sky coverage. Such an observing strategy also favors the detection of stronger sources instead of weaker ones, increasing the number of cross-identifications with flux-limited samples in other wavebands and making radio followup observations easier. For these reasons, we designed the NVSS to use the shortest practical integration times ($\tau \approx 23$ s) and cover the whole sky visible from the VLA. Multiplying the integration time by a factor of four (doubling the sensitivity and decreasing the sky coverage by a factor of four) would have reduced the number of sources detected per unit time by a factor of about 2.5, gaining only 2×10^5 sources with $S < 2.5$ mJy and losing nearly 15×10^5 sources stronger than 2.5 mJy.

Three practical considerations strongly constrain the NVSS observing strategy.
(1) The observing frequency is almost completely determined by technical limitations. At shorter wavelengths ($\lambda \leq 6$ cm) the VLA primary beam is so small that literally millions of snapshots are needed to cover the sky, and no array configuration is compact enough to avoid resolving many sources. At longer wavelengths ($\lambda \geq 90$ cm) the primary beam is so large that multiple snapshots are required for adequate (u, v) coverage in the presence of confusion, and some form of three-dimensional imaging becomes necessary. In addition, the VLA system noise is much higher, the available bandwidth is much lower, and ionospheric phase fluctuations degrade image accuracy.
(2) Only in the compact D and DnC configurations can the full continuum IF (intermediate

frequency) bandwidth (nominally $\Delta\nu = 50$ MHz) be used for maximum sensitivity at 1.4 GHz without excessive bandwidth smearing in the outer portions of the snapshot images. The VLA correlator allows only continuum observations (in contrast to pseudo-continuum spectral line observations) at two widely spaced frequencies (for increased sensitivity and improved (u, v) coverage through bandwidth synthesis) while retaining polarization information. The drawbacks of wideband continuum observations are increased vulnerability to radio-frequency interference, some bandwidth smearing even in the D configuration, and small but significant geometric mapping errors. Detecting and editing data contaminated by interference, correcting for bandwidth smearing, and removing geometric mapping errors are large but manageable computational tasks (see Section 4).

(3) The time window for making sensitive 1.4 GHz surveys may be very narrow. The new L-band VLA receivers were not installed until the summer of 1993; they reduced the system noise by nearly a factor of two. The computing resources for reducing the data at a reasonable cost were not available before 1991. The same technological advances that make the NVSS observations practical now may make them impossible in the future. For example, the 1992 World Radio Administrative Conference (WARC) allocated the 1452 through 1492 MHz band to the Broadcast Satellite Service. This service will broadcast digital audio at power levels sufficient for reception by handheld receivers, and these signals may contaminate or completely obliterate VLA continuum observations within ± 16 MHz of that band. NVSS observations are best made at night to minimize solar interference, artificial interference, and ionospheric Faraday rotation, so a minimum of three VLA configuration cycles are needed to cover all right ascensions. We therefore observed intensively during the three cycles between 1993 September and 1996 October and covered nearly all of the NVSS area successfully, with later observations to fill the few remaining gaps. We thank the other D-configuration users for their patience during this time.

3. Observations

The NVSS uses the pointillist technique to paint a remarkably smooth picture of the whole sky north of $\delta = -40°$ with 217,446 small snapshot images. Section 3.1 outlines the method that we designed for weighting and combining partially overlapping snapshots to obtain large, uniformly sensitive sky images. Section 3.2 describes the NVSS snapshot observations, and section 3.3 summarizes the special calibration scans needed to produce accurate widefield images in both total intensity and linear polarization.

3.1. Uniform Sky Coverage with Discrete Snapshots

The instantaneous sky coverage of the VLA is limited by the primary beam of each antenna. The VLA primary power pattern is approximately a circular Gaussian

$$P(\rho) = \exp\left[-4\ln 2\left(\frac{\rho}{\theta_{\rm P}}\right)^2\right] , \tag{5}$$

where ρ is the angular distance from the pointing position and $\theta_{\rm P}$ is the primary FWHM, about $31'$ at $\nu = 1.4$ GHz. Sky images much larger than $\theta_{\rm P}$ and having nearly uniform sensitivity can be constructed from weighted sums of partially overlapping snapshot images, each covering most of one primary beam area. Since the primary beam is circular and $\theta_{\rm P} \ll 1$ radian, it is obvious (though not easy to prove) that a hexagonal close-packed grid of pointing positions provides the most uniform coverage for a given sky density of snapshots. The optimum angular distance Δ between pointing positions on this grid is a compromise between uniformity ($\Delta \ll \theta_{\rm P}$) and observing efficiency ($\Delta \approx \theta_{\rm P}$) because a larger Δ reduces the number of fields that must be observed and hence the total time spent moving between successive positions.

The brightness B at any point in a large sky image constructed from the weighted sum of brightnesses b_i in the m snapshot images contributing to that point is

$$B = \sum_{i=1}^{m} W_i b_i \bigg/ \sum_{i=1}^{m} W_i \ . \tag{6}$$

The final image sensitivity is maximized if the statistical weight W_i multiplying each input brightness is proportional to the square of the signal-to-noise ratio at that position. For a set of similar snapshots, the signal-to-noise ratio is simply proportional to the primary power gain. Thus we multiplied each snapshot image (which was not corrected for primary-beam attenuation) by the primary power pattern $P(\rho)$ before adding it to the large weighted image. This is equivalent to making the normal correction for primary-beam attenuation [dividing by $P(\rho)$] and then multiplying by $P^2(\rho)$. Simultaneously we added a "weight beam" $W(\rho) = P^2(\rho)$ to the corresponding weight image. The final large sky image is just the ratio of the large weighted image to the large weight image (Equation 6). The sensitivity of the final sky image is everywhere proportional to

$$\left(\sum_{i=1}^{m} W_i\right)^{1/2} . \tag{7}$$

Uniform sensitivity is attained only when the sum of the weight beams, not just the sum of the broader primary beams, is nearly independent of position. The weight beam corresponding to a Gaussian primary beam with FWHM $\theta_{\rm P}$ is also a Gaussian, but its FWHM is only $\theta_{\rm P}/\sqrt{2}$ (Figure 8). The final sky image can have nearly uniform sensitivity only if Δ is not much larger than $\theta_{\rm P}/\sqrt{2} \approx 22'$. We chose $\Delta = 26'$ for the NVSS. The minimum sum of weights is 0.81, so the worst-case sensitivity is about 90% of the sensitivity at pointing centers. Note that the image response is quite uniform; it is only the noise level which varies slightly with position.

The individual snapshot images must be truncated at a finite distance $\rho_{\rm m}$ from the beam axis because the primary gain is poorly measured, frequency dependent, and sensitive to pointing errors at large ρ. The mapping efficiency $\eta_{\rm m}$ defined by

$$\eta_{\rm m} \equiv \int_0^{\rho_{\rm m}} W(\rho)\rho\, d\rho \Big/ \int_0^{\infty} W(\rho)\rho\, d\rho \tag{8}$$

is a quantitative measure of the information retained in the truncated image. It indicates the efficiency with which the observing time is used, and the final rms image noise is proportional to ${\eta_{\rm m}}^{-1/2}$. For a Gaussian primary beam, $\eta_{\rm m} = 1 - \exp[-8\ln 2(\rho_{\rm m}/\theta_{\rm P})^2]$. The conflicting goals of accuracy and high imaging efficiency constrain $\rho_{\rm m}$ to lie in the range $0.7 \lesssim \rho_{\rm m} \lesssim 0.85$. All NVSS snapshot images are truncated at $\rho_{\rm m} = 24' \approx 0.8\theta_{\rm P}$ and have mapping efficiency $\eta_{\rm m} \approx 0.98$. A typical grid of pointing centers and image boundaries is illustrated in Figure 9.

3.2. The NVSS Snapshot Observations

To minimize the time spent moving between successive pointing centers, all survey observations were controlled by a special version of Ken Sowinski's VLA antenna holography program. It requires that all pointing positions lie along columns of constant right ascension and rows of constant declination. Since lines of constant right ascension converge as $\cos\delta$, the ideal hexagonal pattern introduced in Section 3.1 cannot be maintained far from the celestial equator. As the grid spacing in right ascension decreases away from the equator, the spacing in declination can increase. We determined the row separation by requiring that the worst-case final image sensitivity (equivalently, the minimum sum of weights) be independent of declination. As $|\delta|$ increases and $\cos\delta$ falls to $1/\sqrt{3}$ of its initial value, an initially hexagonal pattern distorts and then returns to being hexagonal. Rick White (STScI) suggested dividing the sky into wide declination bands in which $\cos\delta$ falls to half its initial value and each successive band contains half as many columns as its predecessor, and he calculated the common pointing grid used by the NVSS and the B-configuration FIRST survey (Becker *et al.* 1995). All right ascensions on this grid are further constrained to be multiples of $0\overset{\rm m}{.}5$ and all declinations have been rounded to the nearest $0\overset{\prime}{.}1$ so that the position of every field can be specified by an 11-character coordinate name. For example, the field centered on (J2000) $\alpha = 07^{\rm h}40\overset{\rm m}{.}5$, $\delta = +51°59\overset{\prime}{.}6$ is called 07405+51596.

A second practical constraint is that the snapshot duration (equal to the $6\,{}^2\!/_3$ s move time plus dwell time) must be a multiple of 10 s. The shortest duration consistent with a reasonable observing efficiency is 30 s, yielding $\tau = 23\,{}^1\!/_3$ s dwell time. The theoretical rms noise at the pointing center of a snapshot image is (Crane & Napier 1989)

$$\sigma_{\rm n} = \frac{\sqrt{2} k_{\rm B} T_{\rm s}}{\eta_{\rm a}\eta_{\rm c} A\sqrt{N_{\rm b} N_{\rm IF}\tau\Delta\nu}}\ , \tag{9}$$

where $k_{\rm B}$ is the Boltzmann constant, $T_{\rm s}$ is the system temperature ($T_{\rm s} \approx 33$ K at the zenith), $\eta_{\rm a} = 0.51$ is the aperture efficiency at 1.4 GHz, $\eta_{\rm c} = 0.79$ is the VLA continuum correlator efficiency, A is the geometric area of one 25 m telescope, $N_{\rm b} = 351$ is the number of baselines, $N_{\rm IF} = 4$ is the number of continuum IF channels (giving both right and left circular polarizations at nominal sky frequencies 1.3649 and 1.4351 GHz), and $\Delta\nu \approx 42$ MHz is the effective continuum IF bandwidth. Pickup of ground radiation and atmospheric emission both increase the system noise away from the zenith, so we increased the snapshot durations at high zenith angles (see Table 1) to maintain a nearly constant theoretical noise level (Figure 10). The total VLA time, including time for calibration and repeated observations of snapshots ruined by interference, bad weather, and equipment failures, needed to complete the NVSS was about 2700 hours.

Most NVSS observations are sequences of snapshots made within 1 hour of transit along columns of constant right ascension in order to minimize the zenith angle and system noise. The column separation in right ascension, total snapshot duration, array configuration (D or DnC), and hour-angle limits depend on declination, so the survey pointing grid was broken into 14 independently observed declination bands (Table 1). Bands 5 and 7 approach the zenith and must be observed very near transit to avoid excessively long azimuth slews between snapshots. The telescope pointing can settle to within $1'$ during the $6\,{}^2\!/_3$ s move time only if the azimuth slew $\Delta A \lesssim 45'$. For a snapshot at declination δ and hour angle h, the azimuth is

$$A = \sin^{-1}\left\{\frac{-\cos\delta\sin h}{[1-(\cos\Phi\cos\delta\cos h+\sin\Phi\sin\delta)^2]^{1/2}}\right\}\ , \tag{10}$$

where $\Phi = 34^\circ\ 04'\ 44''$ is the VLA geodetic latitude. The upper declination limit of band 5 and the lower declination limit of band 7 were chosen so that $\Delta A \leq 45'$ for all $|h| \leq 12^{\rm m}$. Band 6 ($+25^\circ\ 09'\ 54'' \leq \delta \leq +43^\circ\ 54'\ 42''$) crosses the VLA zenith and was observed about $2^{\rm h}\ 30^{\rm m}$ after transit.

3.3. Calibration Observations

Standard on-axis observations of amplitude, phase, and polarization calibration sources were made during each observing night. The NVSS flux densities are ultimately based on the Baars *et al.* (1977) absolute scale. We monitored our secondary calibrators and compared them with 3C 295, whose flux densities on baselines shorter than 2000λ were taken to be 22.81 Jy at 1364.9 MHz and 21.87 Jy at 1435.1 MHz.

Observations of the strong sources J1833−210, J0521+166 = 3C 138, and J1411+522 = 3C 295 were made at pointing positions offset by $\rho = \pm 5'$, $\pm 10'$, $\pm 15'$, $\pm 20'$, and $\pm 25'$ in both right ascension and declination. We used the resulting images to measure the primary beam power pattern, the amount of bandwidth smearing, and the geometric errors (see Section 4.3) in the uncorrected NVSS snapshot images. The observed primary power pattern (data points in Figure 13) is close to that of a uniformly illuminated circular aperture whose diameter is 24.5 m. The primary voltage pattern is the Bessel function $2J_1(z)/(z)$, where $z \approx 3.234\rho/\theta_{\rm P}$. The data indicate $\theta_{\rm P} = 30.83 \pm 0.07$ arcmin at $\nu = 1.4$ GHz. Images of the data from the two frequency channels (1364.9 and 1435.1 MHz) were also made separately, and the ratio of P, the power in one frequency channel, to $\langle P \rangle$, the average in both channels, is plotted as a function of ρ in Figure 14.

In the "leakage term" model of instrumental polarization, each measured polarization is the nominal instrumental polarization (pure R or L circular for the VLA) plus a complex factor, called the "D term," multiplying the orthogonal polarization. The D terms can be determined from observations of a calibrator at the antenna pointing center. Since most of the calibrators compact enough to be good phase calibrators are time variable, their polarizations are not known *a priori*. This means that the calibration source polarization and the instrumental calibration parameters must be determined simultaneously. For arrays composed of alt-az mounted antennas, a change in parallactic angle has different effects on the interferometer response to source and instrumental polarizations. For sources with unknown polarization, observations spanning a range of parallactic angles can be used to determine all of the unknowns except absolute position angle at the pointing center. If the source polarization of one calibrator is known, then a single observation of that calibrator is sufficient to determine the instrumental polarization at the pointing center. Our on-axis polarization position-angle calibration is based on the linearly polarized source 3C 286, whose electric-vector position angle is 33°.

Special calibration observations were made to determine the variation of instrumental polarization and gain with position in the primary beam. Such variations should be time-independent, so these observations were needed only once per major observing cycle. Holography-mode scans covering the 11×11-point grid of all azimuth and elevation offsets up to $25'$ in multiples of $5'$ were made on several strong point sources, and images based on these scans were used to map the VLA instrumental polarization over the primary beam area. The results demonstrate that the instrumental polarization rotates with parallactic angle as predicted and does not vary significantly with time. The instrumental polarization is also independent of elevation angle, as expected since the change of antenna gain with elevation is $< 0.5\%$ at 1.4 GHz. The data were averaged to yield beam polarization maps showing the total-intensity beam and the fractional circular polarization beam (Figure 11) as well as the fractional Q and U polarization beams (Figure 12). The VLA antennas are asymmetric and have off-axis feeds that respond to the two circular polarizations. The total-intensity beam map is nearly circular with FWHM $= 30.90 \pm 0.15$ arcmin. The V polarization map agrees well (within 1%) with the expected (Chu & Turrin 1973) beam squint. It shows that the circularly polarized beams are separated by $\epsilon = 1.71 \pm 0.02$ arcmin along position angle 134.6 ± 1 deg. While this beam squint is large enough to preclude sensitive circular-polarization imaging, it does not significantly alter the total-intensity beam formed by averaging the two circularly polarized beams. For a separation ϵ between circular Gaussian circularly polarized beams with FWHM $\theta_c \gg \epsilon$, the major axis FWHM θ_M of the total-intensity beam is

$$\frac{\theta_M}{\theta_c} \approx \left[1 + 2\ln 2\left(\frac{\epsilon}{\theta_c}\right)^2\right]^{1/2}, \tag{11}$$

so squint broadens the total-intensity primary beam by only about 4 arcsec.

4. The NVSS Snapshot Images

A VLA snapshot observation is quick but the synthesized beam is dirty. We have written special AIPS tasks and procedures to automate the production of snapshot images, enforce uniform quality standards, and reduce opportunities for human error. The dirty beam has such high sidelobe levels that cleaning must be done very carefully. The low resolution, wideband, widefield NVSS snapshot images cannot be made without stretching or violating many of the usual assumptions behind standard imaging algorithms. We made several first-order corrections to minimize the resulting errors.

4.1. Automated Imaging

The snapshot images were all made by a special AIPS task, VLAD. It reads the calibrated multisource (u,v) data file and successively images all of the survey snapshots from one night's observing. After splitting out the data from one snapshot and applying the calibration table, VLAD flags those correlators having excessively large rms fluctuations among their $3\,{}^1\!/_3$ s samples. This prevents strong interference from corrupting the images. The surviving (u,v) data are time averaged over the snapshot duration and imaged. The main image field is normally a square 512 pixels $\times 12''$ pixel$^{-1} \approx 102'$ on a side to cover the main lobe of the primary beam plus most of the first sidelobe. The (u,v) data are convolved with a spheroidal function that effectively suppresses aliased images inside the field from sources lying outside the field, but it cannot eliminate those sidelobes which do fall inside the image. Outside sources whose flux densities exceed ≈ 2 mJy after attenuation by the primary beam can leave noticeable sidelobes in the main field so they must be imaged and cleaned separately. Figure 15 shows the extended primary-beam response of a uniformly illuminated circular aperture 24.5 m in diameter, a good approximation to the measured VLA primary pattern. VLAD therefore images and cleans additional small fields centered on the positions of all sources whose flux densities exceed the values indicated by the broken curve in Figure 15. It does so by reading a merged list of sources taken from (in order of preference) the Becker *et al.* (1991) catalog of sources found on the 1400 MHz Green Bank sky images, the Parkes-MIT-NRAO 4.85 GHz survey catalogs of sources in the southern (Gregory *et al.* 1994), tropical (Griffith *et al.* 1994), and equatorial (Griffith *et al.* 1995) zones, the 6C 151 MHz north polar catalog (Baldwin *et al.* 1985), and the Parkes PKSCAT90 source list (Wright & Otrupcek 1990).

Clean components from images containing peaks brighter than 100 mJy beam^{-1} are used to phase self-calibrate the (u,v) data, and VLAD automatically performs both amplitude and phase self-calibration on fields containing sources brighter than 400 mJy beam^{-1}. The largest clean components are subtracted from the (u,v) data. Residual amplitudes exceeding half the interference flagging levels indicate deviant data points, which are flagged before the the field is reimaged and recleaned. To minimize the effects of pixel quantization on those images containing a source brighter than 500 mJy beam^{-1}, VLAD measures the position of the brightest peak and reimages at a slightly shifted position so that the brightest peak falls precisely on a pixel center.

The (u, v)-plane coverage of a single VLA snapshot is very poor. Although "natural" weighting theoretically minimizes image noise, the heavy concentration of short VLA baselines produces a broad pedestal under the central peak of the synthesized, or dirty, beam. This pedestal makes cleaning difficult, and the integrated flux densities of extended sources are often affected. In addition, natural weighting produces six very strong diffraction spikes because there are so many intra-arm baselines. We therefore used "super uniform" weighting with UVBOX = 5 (cf. Sramek & Schwab 1989) to alleviate these effects, at a cost of $< 5\%$ increase in image noise. The resulting synthesized beam has a nearly Gaussian main lobe with FWHM about $45''$, small nearby sidelobes with no pedestal (Figure 16), and slightly reduced diffraction spikes (Figure 17). Even so, the amplitudes of these diffraction spikes approach 0.3 of the peak at offsets around 0.3 deg, the grating ring radius corresponding to the shortest D-configuration spacings of about 37 m.

The large diffraction sidelobes must be cleaned very carefully. The cleaning must be fairly deep, lest the residual image fluctuations be dominated by uncleaned sidelobes rather than by receiver noise. Cleaning too deeply causes a new problem, systematic suppression of signals by "clean bias." One aspect of clean bias is already known to VLA users. Since the sidelobes are much broader than the main peak of the dirty beam, the total area under the intersections of the diffraction spikes and the grating ring can be larger than the area under the central peak of the synthesized beam (Figure 17). In a dirty image, an extended source may therefore appear brighter at these intersections than at the correct position, and cleaning will put some clean components onto the six intersections. Each time the synthesized beam response from such a clean component is subtracted from the dirty image, flux is subtracted from the true source position as well. The fraction of the clean component flux erroneously subtracted from the source position is equal to the relative amplitude of the sidelobe, up to 0.3 for the synthesized beam shown in Figure 17. The result is a clean image in which some of the source flux has been moved from the correct position to six ghost images at the intersections of the diffraction spikes with the grating ring. If the dirty image is dominated by a single extended source at the center, the most effective cure for this problem is to restrict cleaning to a small region containing the source but not the grating ring. This cannot normally be done in a survey because there are many sources spread over the whole primary beam, which is much larger than the grating ring. Fortunately, few extragalactic sources are larger in both dimensions than several times the D-configuration synthesized beamwidth $\theta \approx 45''$.

Unfortunately, the largest sidelobes in the snapshot synthesized beam affect even point sources in the presence of noise. It is clear from Figure 17 that the peak corresponding to a strong $(S \gg \sigma)$ point source can easily be located in a dirty image. As cleaning proceeds, the peaks of even the strongest sources in the residual image decrease until they are only a few σ above the sidelobes. The sidelobes cover a much larger area of sky than the main peak, so continued cleaning increases the probability that a positive sidelobe on top of a positive noise fluctuation, or even a negative sidelobe on top of a negative noise fluctuation, exceeds in magnitude the peak at the source position. When this happens, a clean component will be placed on the noisy sidelobe and subtracted. Note that subtracting a positive clean component located on a positive sidelobe and subtracting a negative clean component located on a negative sidelobe will *both* subtract positive flux from the true source position. The consequence is that further cleaning will *systematically* reduce the flux densities of all point sources in the clean image by an amount which is dependent on the image noise and synthesized-beam sidelobe levels, but which is nearly independent of the true source flux density. Unless corrective measures are taken, this clean bias can have an unacceptably large effect on sources in a VLA snapshot survey, reducing their average flux densities by as much as 2σ. If cleaning is carried too far, clean bias eventually reduces even the image noise. It is quite easy to clean a VLA snapshot image to the point that the fluctuations in the clean image are only a tiny fraction of the theoretical noise! Consequently, the rms map fluctuation is not a reliable measure of the noise contribution to the position and flux-density uncertainties of sources appearing in an overcleaned snapshot image.

Clean bias can be reduced but not completely eliminated from widefield snapshot images. The most effective ways to lower clean bias are to (1) minimize the area cleaned, (2) weight the (u, v) data to get a cleaner synthesized beam, (3) stop cleaning while the peak residuals are still well above the rms noise, and (4) reject weak, isolated clean components as likely being due to sidelobes broader than the main peak of the synthesized beam. VLAD implements these measures as follows: The whole 512×512 pixel image is only cleaned down to 1.25 mJy beam^{-1}. Groups of clean components in regions $25''$ in diameter whose absolute summed flux densities are less than 0.5 mJy are not used. Deeper cleaning is limited to a circle of radius $20'$ at the image center. The deeper cleaning is terminated when the peak residual falls to 0.75 mJy beam^{-1}, and isolated components are again rejected as described above. These procedures reduce the average clean bias in the final NVSS images to $\Delta S_{\rm P} \approx -0.3$ mJy beam^{-1} except in very crowded fields. We measured this value of $\Delta S_{\rm P}$ by adding artificial point sources to the (u, v) data and finding the mean difference between their map and input flux densities. Since the magnitude of the clean bias is still smaller than the rms image noise, correcting sources for clean bias yields flux densities whose errors are dominated by noise, not bias. The price paid for restricting clean is higher map "noise" since weak uncleaned sidelobes contribute fluctuations comparable with the thermal noise fluctuations.

Strong sources must be cleaned accurately or improperly subtracted sidelobes from the very dirty synthesized beam will limit the image dynamic range. All NVSS snapshot images are made with pixels much smaller than the beamwidth—there are 3.75 $12''$ pixels per $45''$ beam FWHM. During cleaning, the clean-component flux densities are subtracted from the (u, v) data. At large distances ρ from the pointing center, the primary beam attenuation is different in the IF channels whose sky frequencies are 1.3649 GHz and 1.4351 GHz (Figure 14), so the attenuated flux density of a source in each channel is not equal to the average (1.400 GHz) attenuated flux density. The (u, v) spacings are different at the two frequencies as well, so subtracting the average attenuated flux density would leave large residuals in the (u, v) data at both frequencies. VLAD uses the measured relative attenuations (Figure 14) to subtract the correct attenuated flux density separately at each frequency. It further improves the overall cleaning accuracy by subtracting flux densities calculated from the assumption that all sources have the median spectral index $\langle\alpha\rangle = 0.7$. Sources with exceptionally steep $(\alpha \gg 0.7)$ or inverted $(\alpha < 0)$ spectra are cleaned less accurately. Finally, the beam patch used in the Clark cleaning algorithm (cf. Cornwell & Braun 1989) is twice the dirty image size, so that all sidelobes everywhere in the image are subtracted during each minor cycle.

After the total-intensity images are made, the calibrated and edited (u, v) data are used to make the Q and U linear-polarization images, which require little cleaning and no further self-calibration.

The final (u, v) data for each snapshot, corrected for the frequency dependence of the primary beam and for bandwidth smearing, are stored for possible future use.

The rms brightness fluctuations in most Q and U snapshot images appear to be noise limited in the range 0.25 to 0.30 mJy beam^{-1}. Most total-intensity snapshot images have rms fluctuations between 0.35 and 0.45 mJy beam^{-1}. Some of this excess is caused by the 0.08 mJy beam^{-1} confusion from numerous faint sources unresolved by the $45''$ beam, but most appears to result from imperfect cleaning of stronger sources. Snapshot images containing no sources stronger than 10 mJy frequently have the lowest fluctuation levels while images containing several moderately strong sources, especially if they are near the edge of the primary beam, are noisier. Fields containing sources stronger than about 1 Jy normally have significant residual sidelobes along the dirty-beam diffraction spikes.

4.2. Bandwidth Smearing

The NVSS snapshot observations are made with a nominal IF bandwidth $\Delta\nu \approx 50$ MHz, so sources far from the phase center are significantly blurred by bandwidth smearing. This effect is harmful in the area used to generate the final images (a circle of radius $\rho_{\rm m} = 24'$), where a constant point-source response is desired, but it is actually helpful for suppressing responses to strong sources outside this area. We therefore made a first-order correction for bandwidth smearing which is effective only for $\rho \lesssim \rho_{\rm m}$.

In the image plane, the uncorrected point-source response is the convolution of the unsmeared restoring beam with a radially extended bandwidth-smearing "beam" whose angular profile is the same as the frequency profile of the IF passband and whose angular width is $\rho\Delta\nu/\nu$, where ρ is the angular distance from the phase center. Bandwidth smearing reduces the peak flux density $S_{\rm P}$ of a source but not its integrated flux density $S_{\rm I}$. Variances add under convolution, so the variance of the smeared beam is the sum of $\theta^2/(8\ln 2)$, the variance of the Gaussian restoring beam with FWHM θ, and $(\rho\Delta\nu/\nu)^2/12$, the variance of the bandwidth-smearing beam for a rectangular IF passband of width $\Delta\nu$. For small amounts of bandwidth smearing, the point-source response remains nearly Gaussian, regardless of the detailed profile of the IF passband. Its peak is multiplied by

$$S_{\rm P}/S_{\rm I} \approx \left[1 + \frac{2\ln 2}{3}\left(\frac{\rho\Delta\nu}{\nu\theta}\right)^2\right]^{-1/2} \leq 1 \qquad (12)$$

and its width is divided by $S_{\rm P}/S_{\rm I}$. Equation 12 can be used to define an "effective" rectangular IF bandwidth $\Delta\nu$. To measure the effective bandwidth $\Delta\nu$ of the $\nu = 1.4$ GHz NVSS observations, we observed three strong point sources at radial offsets up to $\rho = 25'$ in the four cardinal directions N, S, E, and W. The data were imaged, cleaned, and restored with $\theta = 45''$ FWHM Gaussian beams. We made Gaussian fits to the strong sources on these images, and the mean ratios $S_{\rm P}/S_{\rm I}$ are shown as filled circles in Figure 18. The continuous line passing through these data was calculated from Equation 12 with the best-fit effective bandwidth $\Delta\nu = 42 \pm 1$ MHz.

In the (u, v) plane, bandwidth smearing can be characterized by the reduction it causes in the fringe visibility V of a unit point source. If the source has direction cosines (l, m) relative to the phase reference position and is observed on a baseline having projected lengths (u, v), then the delay on that baseline is $\tau = (ul + vm)/c$ and the smeared visibility is

$$V(\tau) = \left[\frac{\sin(\pi\tau\Delta\nu)}{\pi\tau\Delta\nu}\right] e^{i2\pi\tau\nu} \ . \qquad (13)$$

The visibility amplitude is multiplied by the factor $r(\tau) = {\rm sinc}(\tau\Delta\nu) \leq 1$ at the correlator output, but the noise is not. Dividing the amplitude by $r(\tau)$ during the imaging process eliminates the bandwidth smearing, but it also divides the noise on that visibility by $r(\tau)$. Very large corrections for bandwidth smearing yield unacceptably noisy images.

We implemented the following procedure to reduce bandwidth smearing: (1) Subtract the clean components from the (u, v) data used to make a normal (smeared) clean image. Treat all clean components as if they were produced by point sources at the component positions. (2) For each clean component and each fringe visibility, calculate $r(\tau)$. (3) Divide the clean-component flux density by the larger of $r(\tau)$ or the limit $(1.25)^{-1}$ and add this corrected flux density to the residual visibility. (4) Make the corrected image from these corrected visibilities. We tested the efficacy of this procedure by imaging strong point sources observed far from the phase reference position, and the results are shown by the open circles in Figure 18. Bandwidth smearing has been almost completely eliminated up to $\rho \approx 15'$ from the phase center. Since the snapshot image weight (Figure 13) is very low for $\rho > 15'$, strong point sources in the final weighted NVSS images should have $S_{\rm P}/S_{\rm I} > 0.98$ everywhere. This limited bandwidth-smearing correction increases the rms noise by $\leq 2\%$ even if a strong point source is present far from the phase reference position.

4.3. Four Geometric Errors and Their Corrections

A computationally expensive three-dimensional Fourier transform of the three-dimensional (u, v, w) visibility data is formally required to image any finite portion of the spherical sky away from the instrumental zenith (cf. Perley 1989). Since the VLA baselines are nearly horizontal, the VLA is instantaneously almost coplanar. The usual two-dimensional transform of the (u, v) data can be used to make a widefield image from a single snapshot observation, but the direction cosines (l', m') in the resulting image differ slightly from the correct values (l, m):

$$l' = l + (\sqrt{1 - l^2 - m^2} - 1) \tan Z \sin \chi \tag{14a}$$

$$m' = m - (\sqrt{1 - l^2 - m^2} - 1) \tan Z \cos \chi \; . \tag{14b}$$

Here Z is the zenith angle and χ is the parallactic angle of the phase reference position during the snapshot. For small angular displacements ρ from the phase center, $(\sqrt{1 - l^2 - m^2} - 1) \approx -\rho^2/2$, and the distortion caused by imaging with a two-dimensional Fourier transform pulls each source toward the zenith by an amount proportional to the square of its distance from the phase center. Circles on the sky remain circles with the same diameters on the images, but their centers are offset as illustrated by Figure 19. This distortion causes position errors as large as $18''$ at the edges of the southernmost NVSS snapshot images. We therefore recorded the zenith and parallactic angles of all snapshot images and used Equation 14 to correct the image distortions geometrically.

The VLA is not parallel to the equatorial plane, so snapshots made at different hour angles yield images with different distortions. Multiple snapshots cannot be imaged with two-dimensional transforms and deconvolved simultaneously to yield better (u, v)-plane coverage and lower sidelobes. In contrast, an east-west array such as the WSRT is always coplanar, and widefield full-synthesis images can be made with two-dimensional Fourier transforms. Thus the WENSS has superior (u, v)-plane coverage and lower sidelobes, at the expense of longer observing times per field and north-south beamwidth proportional to $1/\sin(\delta)$. The WSRT is better suited to polar surveys at lower frequencies (for fewer and larger primary beam areas), while the VLA is able to reach low declinations with constant resolution and at higher sky frequencies.

The (receiver gain weighted) centroid frequency $\nu_{\rm c}$ of each VLA continuum IF channel is slightly lower than the nominal frequency ν_0 (1364.9 or 1435.1 MHz) used to calculate the (u, v) coordinates. This difference uniformly shrinks all image dimensions by the factor $\nu_{\rm c}/\nu_0$ about the phase reference position. To measure this radial scaling of images made with data from both IF channels, we observed several strong point sources at offset phase-reference positions and imaged them. We compared their positions in pairs of images having symmetric offsets to distinguish this symmetric scaling error from the antisymmetric position errors described by Equation 14. The measured image distances $\rho_{\rm m}$ divided by the true distances ρ from the phase reference position are

$$\left(\frac{\rho_{\rm m}}{\rho}\right) = \left(\frac{\nu_{\rm c}}{\nu_0}\right) = 0.9962 \pm 0.0001 \; . \tag{15}$$

The (signal weighted) centroid frequency also varies across the primary beam because the width of the primary power pattern scales as ν^{-1}, so $P(\rho, \nu) \approx P(\rho\nu)$. Even if the IF passband were rectangular and centered on frequency ν_0, multiplication of the received signal by the primary power pattern would multiply the effective centroid frequency and shrink the image by a second scaling factor

$$\left(\frac{\rho_{\rm m}}{\rho}\right) = \int_{\nu_0-\Delta\nu/2}^{\nu_0+\Delta\nu/2} \nu P(\rho\nu)\ d\nu \Big/ \int_{\nu_0-\Delta\nu/2}^{\nu_0+\Delta\nu/2} \nu_0 P(\rho\nu)\ d\nu\ , \tag{16}$$

where $\Delta\nu$ is the IF bandwidth. In the limit $\Delta\nu/\nu_0 \ll 1$,

$$P(\rho\nu) \approx P(\rho\nu_0) + (\nu - \nu_0)\frac{\partial P(\rho\nu)}{\partial\nu}\bigg|_{\nu=\nu_0} \tag{17}$$

and the radial coordinate error is

$$(\rho_{\rm m} - \rho) \approx \frac{(\Delta\nu)^2}{12\nu_0}\frac{\partial \ln P(\rho\nu)}{\partial\nu}\bigg|_{\nu=\nu_0}\ . \tag{18}$$

For a Gaussian primary beam with FWHM $\theta_{\rm P}$ at frequency ν_0,

$$(\rho_{\rm m} - \rho) \approx -\frac{2\ln 2}{3}\left(\frac{\rho\Delta\nu}{\theta_{\rm P}\nu_0}\right)^2\ . \tag{19}$$

Figure 20 shows the position errors $(\rho_{\rm m} - \rho)$ for a Gaussian primary beam (dotted curve), the primary beam of a uniformly illuminated circular aperture (dashed curve), and the error calculated from Equation 18 and the values of $\partial \ln P/\partial\nu$ indicated by Figure 14 (continuous curve).

A third radial distortion occurs when the snapshot images are multiplied by the primary power pattern $P(\rho)$ (see Section 3.1) because the FWHM θ of the Gaussian synthesized beam is a finite fraction of the primary beamwidth $\theta_{\rm P}$. Before multiplication by $P(\rho)$, the image response to a point source offset by $\rho = \rho_0$ from the pointing center is

$$G(\rho - \rho_0) = \exp\left[-4\ln 2\left(\frac{\rho - \rho_0}{\theta}\right)^2\right]\ , \tag{20}$$

and its centroid is at the correct radial offset ρ_0. After multiplication by $P(\rho)$, the image centroid offset $\rho_{\rm m}$ is shifted to

$$\rho_m = \rho_0 + \int (\rho - \rho_0) G(\rho - \rho_0) P(\rho)\ d\rho \Big/ \int G(\rho - \rho_0) P(\rho)\ d\rho\ . \tag{21}$$

In the limit $\theta/\theta_{\rm P} \ll 1$, we can expand the primary power pattern near $\rho = \rho_0$:

$$P(\rho) \approx P(\rho_0) + (\rho - \rho_0)\frac{dP(\rho)}{d\rho}\bigg|_{\rho=\rho_0}\ . \tag{22}$$

Inserting this expansion into Equation 21 yields the radial position error caused by the primary-beam correction:

$$(\rho_m - \rho) \approx \frac{\theta^2}{8\ln 2}\frac{d\ln P(\rho)}{d\rho}\ . \tag{23}$$

For a Gaussian primary beam with FWHM $\theta_{\rm P}$, Equation 23 reduces to $(\rho_{\rm m} - \rho) \approx -\rho(\theta/\theta_{\rm P})^2$, a linear scaling shown by the dotted line in Figure 21. Applying Equation 23 to the primary pattern of a uniformly illuminated circular aperture gives the dashed curve in Figure 21. We measured the position shifts caused by weighting using offset snapshot observations of strong point sources; the results are also shown in Figure 21.

The effects of these four geometric errors and their corrections are illustrated by Figure 22. Snapshot observations displaced $\rho = 5$, 10, 15, 20, and 25 arcmin N, S, E, and W from the southern calibration source J1833−210 were made near transit ($Z \approx 55°$, $\chi \approx 180°$). The source positions were measured from Gaussian fits on the resulting images before (open circles) and after (filled circles) the corrections were applied. Small crosses indicate the true offsets $\Delta\alpha$, $\Delta\delta$. The plotted units are arcmin for the true offsets and arcsec for the errors in order to magnify the small errors. The open circles are pulled upward toward the zenith (Equation 14) and inward toward the image center by the two frequency centroid errors (Equations 15 and 18) as well as by weighting (Equation 23). After correction, the residual errors are all $< 1''$.

4.4. Widefield Polarization Corrections

The spurious instrumental response is the product of the complex fractional polarization pattern (Figure 12) and the total-intensity image. The instrumental polarization pattern is fixed to the antennas and rotates on the sky as the alt-azimuth mounted antennas track a celestial position. During a single snapshot observation, this rotation (by the parallactic angle of the pointing center) is nearly constant, and the beam polarization images can be rotated by the parallactic angle to match the orientation of the observation on the sky plane. The standard on-axis polarization calibration will have rotated the instrumental polarization vector by minus the sum of the parallactic angles to remove the effects of parallactic angle from the source polarization. The on-axis calibration can be undone by rotating the instrumental polarization images by plus the sum of the parallactic angles. For a single snapshot image, the off-axis instrumental polarization can be corrected by rotating the beam polarization images twice as described above, multiplying by the total-intensity image, and subtracting from the uncorrected polarization images. Extensive tests of this procedure using data from raster scans on strong sources indicate that the residual linear polarization should be $< 0.3\%$ rms in the NVSS images (Cotton 1994).

4.5. Faraday Rotation Limits

Differential Faraday rotation within and between the two wide NVSS passbands partially suppresses the linearly polarized brightness observed in the calibrated polarization images. The passbands can be approximated by two rectangles of width $\Delta\nu = 42$ MHz centered on 1364.9 and 1435.1 MHz. Figure 23 shows the ratio P/P_0 of image to true polarized brightness for images made with data from both IF channels (continuous curve) and from each IF channel alone (broken curves). Beating between the two IF channels reduces the polarization sensitivity of the NVSS Q and U images to almost zero at absolute rotation measure $|RM| \approx 340$ rad m^{-2}. Simard-Normandin *et al.* (1981) determined the rotation measures of 555 extragalactic sources over a wide range of galactic latitudes and found that only eight had rotation measures $|RM| > 340$ rad m^{-2}. In their sample 96% of the sources have $|RM| < 220$ rad m^{-2} ($P/P_0 > 0.5$) and 87% have $|RM| < 90$ rad m^{-2} ($P/P_0 > 0.9$).

5. NVSS Data Products and Analysis Software

The principal data products of the NVSS are (1) a set of 2326 image cubes, each covering $4° \times 4°$ and having three planes containing the Stokes I, Q, and U images, and (2) a catalog of discrete source components found on these images. Software for viewing NVSS images, extracting "postage stamp" subimages, and selecting sources from the catalog is provided via the NRAO home page on the World Wide Web (Condon *et al.* 1998). In addition, the original (u, v) data, the individual snapshot images, and the calibrated (u, v) data used to make them have been archived on tape and are available on request.

Six examples of NVSS postage-stamp images are displayed in Figure 24. The upper left frame shows the radio star HD 23478. The 3σ position error ellipse of the associated IRAS source F03435+3208 is also plotted. The timing position of the pulsar PSR J0628−2800 is indicated by the cross in the upper right frame; the NVSS detects this pulsar as a continuum source. Most known planetary nebulae were detected by the NVSS; the left frame in the middle row displays the diffuse planetary nebula G118.8−74.7. A significant fraction of the extragalactic X-ray sources listed in the ROSAT 1RXS catalog (Voges *et al.* 1997) are NVSS sources (right frame in the middle row). The 3σ X-ray error box is marked by a cross. The more accurate NVSS positions can help resolve ambiguous optical identifications. The lower left frame shows the spiral galaxy NGC 4736. Its NVSS integrated flux density $S = 273 \pm 9$ mJy agrees well with the WSRT 1412 MHz flux density $S = 270 \pm 20$ mJy (de Bruyn 1977), but the NVSS flux densities of significantly larger sources are often too low. The lower right frame contains the position error ellipse of the faint IRAS source F00022+2750. The NVSS "source" near the upper edge of the ellipse is too faint to appear in the catalog, but its coincidence with both the IRAS source and a galaxy suggests that it is real. The NVSS images can be used with caution to find similar sources below the catalog limit.

5.1. The $4° \times 4°$ Image Set

The individual snapshot images are too small and too numerous (217,446) for convenient use, and they must be weighted and combined for uniformly sensitive sky coverage. We therefore divided the sky into a smaller number (2326) of larger ($4° \times 4°$) partially overlapping squares, each of which can be covered by an image 1024 pixels × 15 arcsec pixel^{-1} $\approx 4\overset{\circ}{.}3$ on a side. The exact J2000 image center coordinates (α_0, δ_0) are listed in Table 2, and the image boundaries are plotted in Figure 25. Each image has a name of the form PHHMMSDD, where the prefix is C for a "cube" containing three planes (Stokes I, Q, and U) or I for a simple total-intensity image, HHMM are the hours and minutes of right ascension, the sign of the declination is either P for + or M for −, and DD gives the degrees of declination at the image center. For example, the image cube centered on J2000 $\alpha = 09^{\rm h}45^{\rm m}$, $\delta = +72^\circ$ is called C0945P72. These images are all sine projections tangent to pixel ($x_0 = 512$, $y_0 = 513$), so the relation between pixel coordinates (x, y) and J2000 sky coordinates (α, δ) is (Greisen 1983)

$$x = x_o - \cos\delta\sin(\alpha - \alpha_0)/\epsilon \tag{24a}$$

$$y = y_0 + [\sin\delta\cos\delta_0 - \cos\delta\sin\delta_0\cos(\alpha-\alpha_0)]/\epsilon\ , \tag{24b}$$

where $\epsilon = \pi/43200$ radians $= 15''$ is the pixel separation. Table 2 and Equation 24 fully specify the location on the NVSS image set of any J2000 position with $\delta \geq -40^\circ$.

We constructed each large image by applying the geometric corrections described in Section 4.3 to all of the overlapping weighted snapshot images, regridding the snapshot images to the geometry specified by Equation 24, applying the polarization corrections, and adding the snapshot images to the large weighted image. Simultaneously, a large weight image was constructed. The final image is their ratio, subject to the constraint that the summed weight be at least $0.81 = 0.9^2$. Pixels with lower weight have been blanked to eliminate regions with inadequate coverage and poor sensitivity. All of the single-source (u, v) data sets used to make the snapshot images that contribute to one large image were combined to make one multisource (u, v) file.

Users should keep the following image characteristics in mind: The brightness distribution, also known as the $P(D)$ distribution, of a typical total-intensity image is shown in Figure 26. The rms fluctuation level is $\sigma \approx 0.45$ mJy beam^{-1} for total-intensity images and $\sigma \approx 0.29$ mJy beam^{-1} for the polarization images. The raw Gaussian-fitted peak flux densities $S_{\rm P}$ of point sources on the images should be corrected by subtracting the fitting bias $\Delta S_{\rm P} \approx +\sigma^2/S_{\rm P}$ and the clean bias $\Delta S_{\rm P} \approx -0.3$ mJy beam^{-1}. The rms fluctuations are somewhat larger near strong sources whose sidelobe responses are not completely removed by cleaning. The local dynamic range of the total-intensity images is about 1000:1. Thus sources closer than about $35'$ to a strong source of flux density S and weaker than $10^{-3}S$ may only be sidelobes, especially if they appear to lie on diffraction spikes of the dirty beam. Significant integrated flux may be missing from sources which are extended more than a few times the beamwidth ($45''$ FWHM) in two dimensions. The galactic polarization is too complex to be imaged accurately by VLA snapshots. Near the galactic plane the NVSS polarization images are noisy and extended features are not accurately represented. Surveys with much better (u, v)-plane coverage at short spacings, such as the WENSS (Rengelink *et al.* 1997), are required to image galactic polarization. Finally, the images appear to have small average coordinate offsets $\langle\Delta\alpha\rangle = +0\rlap{.}''025 \pm 0\rlap{.}''022$ and $\langle\Delta\delta\rangle = -0\rlap{.}''113 \pm 0\rlap{.}''027$ (see Sec. 5.2.3). These offsets should be subtracted from uncorrected positions of Gaussian source fits on the NVSS images.

5.2. The NVSS Source Catalog

Most of the information on the NVSS total-intensity images is well represented by elliptical Gaussian fits because the NVSS point-source response ($\theta = 45''$ FWHM) is much larger than the median angular size of extragalactic sources. Even relatively large structures can usually be approximated by a few elliptical Gaussians. Figure 27 shows a portion of one NVSS image containing a very extended triple source plus a number of smaller sources, a model of this area built from a small number of elliptical Gaussians, and the residual difference between the image and the model. Many users will find it easier to use the NVSS catalog of "sources" (actually, elliptical Gaussians, most but not all of which are individual sources) and their fitted parameters than to use the images directly.

5.2.1. The Raw Catalog

A special Gaussian fitting program (VSAD) was written to fit multiple Gaussians to the peaks on each $4° \times 4°$ total-intensity image. The free parameters of each Gaussian are its equinox J2000 central right ascension α (deg) and declination δ (deg), peak amplitude $A_{\rm P}$ (Jy beam^{-1}) above the image zero level (no baseplane was fitted), major-axis FWHM diameter $\theta_{\rm M}$ (deg), minor-axis FWHM diameter $\theta_{\rm m}$ (deg), and major-axis position angle PA (deg east of north). However, the solutions are constrained to prevent fitted diameters smaller than $45''$, the restoring beam size. No single Gaussian was allowed to have $\theta_{\rm M} > 135''$. If the residual in the area covered by a single Gaussian fit was too high, two, three, or even four Gaussians were fit simultaneously. All peaks brighter than 1.5 mJy beam^{-1} were eventually fitted, but only those components with fitted peak brightnesses at least 2 mJy beam^{-1} were kept in the image catalog. There are about 800 fitted components on a typical NVSS total-intensity image. We used the pixel brightness distribution of each image to estimate the "rms" noise plus confusion σ. To minimize the contribution of strong radio sources, we actually measured the semi-interhexile range of the brightness distribution. This is half the brightness range separating the brightnesses of the pixels in the bottom sixth of the distribution from the pixels in the upper sixth. The semi-interhexile range is very nearly equal to the rms for a Gaussian distribution, but it is much less sensitive to the tails of extended distributions.

No Gaussians were fit to the polarized images, which may contain both positive and negative signals. We estimated the raw Q and U polarized brightnesses (Jy beam^{-1}) of all sources detected on the total-intensity images by interpolation at the source positions.

The individual image catalogs were combined and edited to delete duplicate fits from partially overlapping images. The merged NVSS catalog is sorted by J2000 right ascension and is stored in FITS binary table format (Cotton *et al.* 1995). This "raw" catalog contains only the fitted parameters listed above, uncorrected for known biases. It should not normally be used unless corrections are applied to it by the user.

5.2.2. The Corrected User Versions of the Catalog

Two fully corrected user versions of the catalog are available through the program NVSSlist or the NVSS catalog browser (Condon *et al.* 1998). They are generated on-the-fly from the raw catalog and contain derived quantities (e.g., deconvolved source sizes) corrected for known biases. The "fitted" version gives the peak flux density, the fitted major-axis and minor-axis FWHM angular diameters, the major-axis position angle, and the linearly polarized brightness at each source position. The "deconvolved" version gives the integrated flux density, the source major-axis and minor-axis diameters or their upper limits, and an estimate of the linearly polarized flux density. The deconvolved version should be used for most astronomical investigations.

The uncertainties in these parameters are also calculated. No catalog of this size is trustworthy without (1) a theoretical error analysis to enumerate the likely sources of error and derive their functional forms and (2) external verification, preferably via better observations, to confirm the analysis and to check the catalog itself for completeness and reliability. Although many factors contribute to the errors, most can be grouped into just two independent classes—"calibration" errors and "noiselike" errors—which differ in their dependences on source strength. The total uncertainty in each source parameter is normally the quadratic sum of the calibration and noiselike terms. Calibration errors affect even the strongest sources, while noise and confusion dominate the uncertainties in weak-source parameters. Furthermore, calibration errors usually cannot be determined from the survey images alone; they must be deduced from special calibration checks or external data. Noiselike errors are more amenable to statistical analysis based on the measured noise and confusion fluctuations in the survey images. The NVSS noiselike errors were calculated from the Condon (1997) error-propagation model for Gaussian fits.

5.2.3. Positions

The NVSS catalogs return equatorial coordinates α, δ at epoch 1995 ± 2 and equinox B1900, B1950, or J2000. Except in the raw catalog, these positions are corrected for the small image offsets $\langle\Delta\alpha\rangle$, $\langle\Delta\delta\rangle$ discussed in this section. They also return the rms position uncertainties σ_α, σ_δ.

The rms uncertainties σ_α, σ_δ in the centroid coordinates α, δ of any source with uncorrected peak amplitude A_{P} can be approximated by quadratic sums of intensity-independent calibration uncertainties ϵ_α, ϵ_δ and noiselike uncertaintiess that are inversely proportional to A_{P}. The rms noiselike uncertaintiess σ_{M} and σ_{m} parallel to the fitted FWHM major and minor axes θ_{M} and θ_{m} are

$$\frac{\sigma_{\mathrm{M}}^2}{\theta_{\mathrm{M}}^2} = \frac{\sigma_{\mathrm{m}}^2}{\theta_{\mathrm{m}}^2} \approx \frac{1}{(2\ln 2)\rho^2} \ , \tag{25}$$

where ρ is the effective signal-to-noise ratio. If the image noise has a Gaussian correlation length whose FWHM $\theta_{\rm N}$ is comparable with the FWHM clean beam θ, then

$$\rho^2 = \frac{\theta_{\rm M}\theta_{\rm m}}{4\theta_{\rm N}^2}\left[1+\left(\frac{\theta_{\rm N}}{\theta_{\rm M}}\right)^2\right]^{\alpha_{\rm M}}\left[1+\left(\frac{\theta_{\rm N}}{\theta_{\rm m}}\right)^2\right]^{\alpha_{\rm m}}\frac{A_{\rm P}^2}{\sigma^2}. \tag{26}$$

Here $\sigma \approx 0.45$ mJy beam^{-1} is the typical rms noise plus confusion in the NVSS total-intensity images. The exponents empirically determined with a Gaussian noise correlation function are $\alpha_{\rm M} = 5/2$, $\alpha_{\rm m} = 1/2$ for calculating $\sigma_{\rm M}$ and $\alpha_{\rm M} = 1/2$, $\alpha_{\rm m} = 5/2$ for calculating $\sigma_{\rm m}$ (Condon 1997). Note that the variances in Equation 25 are actually twice the theoretical values (Condon 1997). This increase is necessary because the very dirty synthesized beam of a VLA snapshot results in noise and confusion fluctuations correlated on scales much larger than $\theta = 45''$. When projected onto the right ascension and declination axes, the total rms position errors become:

$$\sigma_\alpha^2 \approx \epsilon_\alpha^2 + \sigma_{\rm M}^2\sin^2(PA) + \sigma_{\rm m}^2\cos^2(PA) \tag{27a}$$

$$\sigma_\delta^2 \approx \epsilon_\delta^2 + \sigma_{\rm M}^2\cos^2(PA) + \sigma_{\rm m}^2\sin^2(PA). \tag{27b}$$

The mean image offsets $\langle\Delta\alpha\rangle$, $\langle\Delta\delta\rangle$ and rms calibration uncertainties ϵ_α, ϵ_δ are best determined by comparison with extremely accurate positions of sources strong enough that the noise plus confusion terms in Equation 27 are much smaller than the calibration terms. We used the uncorrected NVSS catalog positions of 419 compact sources stronger than 200 mJy in the 1997 August version of the USNO radio reference frame (Johnston *et al.* 1995). Their offsets $\Delta\alpha$ and $\Delta\delta$ are shown in Figure 28. The mean NVSS image offsets are $\langle\Delta\alpha\rangle = +0\farcs025 \pm 0\farcs022$ and $\langle\Delta\delta\rangle = -0\farcs113 \pm 0\farcs027$. These image offsets remain in the raw NVSS catalog, but they have been removed from the NVSS user catalog positions, which are therefore centered precisely on the USNO reference frame. The rms offsets indicate the NVSS position calibration errors, which are $\epsilon_\alpha = 0\farcs45$ in right ascension and $\epsilon_\delta = 0\farcs56$ in declination, with no significant position dependence. Their small values confirm that the geometric corrections described in Section 4.3 are both accurate and sufficient.

The noise and confusion components dominate the position uncertainties at low ($S < 15$ mJy) flux densities. To verify that the NVSS catalog uncertainties are realistic, we randomly picked four areas containing a total of 244 sources with $2 < S < 10$ mJy from the VLA B-configuration FIRST survey catalog (White *et al.* 1997) and found the NVSS position offsets. The FIRST position errors of these faint sources are much smaller than the NVSS position errors, so the offsets are good estimates of the NVSS errors alone. Figure 29 shows these offsets $\Delta\alpha$, $\Delta\delta$ normalized by the uncertainties σ_α, σ_δ from Equation 27 . The normalized offsets have nearly unit rms scatter, verifying that the NVSS catalog uncertainties are accurate for weak sources. Many of these sources are slightly extended, so the low-resolution NVSS centroid positions might have small intrinsic offsets from the high-resolution ($5''$ FWHM) FIRST positions which favor the compact radio cores that usually coincide with optical identifications. Thus the NVSS catalog position uncertainties for weak sources include any possible offsets between the source centroids and cores. They can be used directly in Equations 2 and 3 to estimate the completeness and reliability of NVSS optical identifications. The typical rms position uncertainties σ_α, σ_δ of unresolved NVSS sources are plotted as functions of flux density in Figure 30.

5.2.4. Angular Sizes

The NVSS point-source response is a circular Gaussian with FWHM $\theta = 45''$ everywhere, so the deconvolved FWHM source sizes $\phi_{\rm M}$ and $\phi_{\rm m}$ are simply

$$\phi_{\rm M} = (\theta_{\rm M}^2 - \theta^2)^{1/2} \tag{28a}$$

$$\phi_{\rm m} = (\theta_{\rm m}^2 - \theta^2)^{1/2} \ , \tag{28b}$$

where $\theta_{\rm M}$ and $\theta_{\rm m}$ are the fitted FWHM sizes. The source major-axis position angle equals the fitted major-axis position angle PA. The fitting constraints $\theta_{\rm M} \geq \theta$ and $\theta_{\rm m} \geq \theta$ (Section 5.2.1) guarantee that $\phi_{\rm M} \geq 0$ and $\phi_{\rm m} \geq 0$ for all sources.

Errors in the fitted sizes are Gaussian distributed with variances

$$\sigma^2(\theta_{\rm M}) = \frac{2\theta_{\rm M}^2}{\rho^2} + \epsilon_\theta^2 \theta^2 \tag{29a}$$

$$\sigma^2(\theta_{\rm m}) = \frac{2\theta_{\rm m}^2}{\rho^2} + \epsilon_\theta^2 \theta^2 \ , \tag{29b}$$

where the exponents $\alpha_{\rm M} = 5/2$, $\alpha_{\rm m} = 1/2$ should be used in Equation 26 for the major axis and $\alpha_{\rm M} = 1/2$, $\alpha_{\rm m} = 5/2$ for the minor axis. The calibration uncertainty $\epsilon_\theta \approx 0.02$ was conservatively estimated from fits to strong flat-spectrum sources assumed to be completely unresolved. It results from a combination of phase errors in the (u, v) data and residual bandwidth smearing (Section 4.2). The probability that the fitted $\theta_{\rm M}$ of a true point source would exceed the beam size θ by more than $2.33\sigma(\theta_{\rm M})$ is only 2%, so we use this criterion to decide whether that axis is significantly resolved. If the major axis is significantly resolved, we calculate its position angle PA and the rms uncertainty $\sigma_{\rm PA}$. Both the fitted and deconvolved major-axis position angles have the same rms uncertainty given by

$$\sigma_{\rm PA}^2 = \frac{4}{\rho^2}\left(\frac{\theta_{\rm M}\theta_{\rm m}}{\theta_{\rm M}^2 - \theta_{\rm m}^2}\right)^2 \ . \tag{30}$$

The exponents $\alpha_{\rm m} = 5/2$ and $\alpha_{\rm M} = 1/2$ should be used in Equation 26 to calculate ρ.

The error distributions of the deconvolved source sizes are neither Gaussian nor symmetric. A convenient statistic to describe them is the pseudo-rms defined as the change in deconvolved source size produced by a change of one standard deviation in the fitted size, whose errors are Gaussian distributed. Adding one standard deviation to the fitted size gives

$$\sigma_+(\phi_{\rm M}) = \{[\theta_{\rm M} + \sigma(\theta_{\rm M})]^2 - \theta^2\}^{1/2} - \phi_{\rm M} \tag{31a}$$

$$\sigma_+(\phi_{\rm m}) = \{[\theta_{\rm m} + \sigma(\theta_{\rm m})]^2 - \theta^2\}^{1/2} - \phi_{\rm m} \tag{31b}$$

and subtracting one standard deviation gives

$$\sigma_-(\phi_{\rm M}) = \phi_{\rm M} - \{[\theta_{\rm M} - \sigma(\theta_{\rm M})]^2 - \theta^2\}^{1/2} \tag{32a}$$

$$\sigma_-(\phi_{\rm m}) = \phi_{\rm m} - \{[\theta_{\rm m} - \sigma(\theta_{\rm m})]^2 - \theta^2\}^{1/2} \ . \tag{32b}$$

Since two-thirds of the area under a Gaussian distribution is bounded by ± 1 standard deviation, two-thirds of the estimates of $\phi_{\rm M}$ or $\phi_{\rm m}$ should be high by less than $\sigma_+(\phi_{\rm M})$ or $\sigma_+(\phi_{\rm m})$ and low by less than $\sigma_-(\phi_{\rm M})$ or $\sigma_-(\phi_{\rm m})$. For significantly resolved sources, the error distributions of deconvolved sizes are not too asymmetric. Thus the deconvolved version of the NVSS catalog characterizes the rms uncertainties in $\phi_{\rm M}$ and $\phi_{\rm m}$ by the averages

$$\sigma(\phi_{\rm M}) = [\sigma_+(\phi_{\rm M}) + \sigma_-(\phi_{\rm M})]/2 \tag{33a}$$

$$\sigma(\phi_{\rm m}) = [\sigma_+(\phi_{\rm m}) + \sigma_-(\phi_{\rm m})]/2 \ . \tag{33b}$$

If one or both axes are not significantly resolved, the deconvolved catalog lists the 98% confidence upper limits to the corresponding source size(s).

5.2.5. *Flux Densities*

The fitted peak amplitude $A_{\rm P}$ must be corrected for two biases: (1) a general fitting bias $\Delta A \approx \sigma^2/A$ caused by noise fluctuations pulling the fitted peak in the direction of the local noise gradient and (2) the NVSS clean bias (Section 4.1) $\Delta A \approx -0.3$ mJy beam^{-1} to yield the corrected peak amplitude A:

$$A = A_{\rm P} - \sigma^2/A_{\rm P} + 0.3 \text{ mJy beam}^{-1}. \tag{34}$$

The rms uncertainty in the corrected amplitude is the quadratic sum of an intensity-proportional calibration uncertainty $\epsilon_{\rm A} A$, a noise uncertainty, and an uncertainty in the bias correction. The NVSS intensity-proportional calibration uncertainty is $\epsilon_{\rm A} \approx 0.03$ or less. To calculate ρ for flux densities, use $\alpha_{\rm M} = \alpha_{\rm m} = 3/2$ in Equation 26. To be conservative, we assume that the rms uncertainty in the bias correction is $\sigma_{\rm B} \approx 0.3$ mJy beam^{-1}, the magnitude of the clean bias correction. The noise uncertainty depends on the number of degrees of freedom allowed in the Gaussian fit. Consequently, the optimum flux-density estimates depend on whether the source is significantly resolved or not (Condon 1997). There are three possibilities:

(1) If a source is significantly resolved in two dimensions, its integrated flux density is

$$I = A\left(\frac{\theta_{\rm M}\theta_{\rm m}}{\theta^2}\right) \ . \tag{35}$$

The rms uncertainty in I is

$$\frac{\sigma_{\rm I}^2}{I^2} \approx \frac{\sigma_{\rm A}^2}{A^2} + \left(\frac{\theta_{\rm N}^2}{\theta_{\rm M}\theta_{\rm m}}\right)\left[\frac{\sigma^2(\theta_{\rm M})}{\theta_{\rm M}^2} + \frac{\sigma^2(\theta_{\rm m})}{\theta_{\rm m}^2}\right] . \tag{36a}$$

Since both the major and minor axes are free parameters,

$$\sigma_{\rm A}^2 \approx \epsilon_{\rm A}^2 A^2 + \frac{2A^2}{\rho^2} + \sigma_{\rm B}^2 \ . \tag{37}$$

(2) If only the major axis is significantly resolved, the best estimate of the source peak amplitude is

$$A^\dagger \equiv A\left(\frac{\theta_{\rm m}}{\theta}\right)^{1/2} , \tag{38}$$

where $\theta = 45''$ is the FWHM point-source response. Its rms uncertainty is

$$\sigma_{\rm A^\dagger}^2 \approx \epsilon_{\rm A}^2 (A^\dagger)^2 + \frac{3(A^\dagger)^2}{2\rho^2} + \sigma_{\rm B}^2 \ . \tag{39}$$

The integrated flux density is

$$I = A^\dagger\left(\frac{\theta_{\rm M}}{\theta}\right) \tag{40}$$

and its rms uncertainty is

$$\frac{\sigma_{\rm I}^2}{I^2} \approx \frac{\sigma_{\rm A^\dagger}^2}{(A^\dagger)^2} + \left(\frac{\theta}{\theta_{\rm M}}\right)\frac{\sigma^2(\theta_{\rm M})}{\theta_{\rm M}^2} \ . \tag{41}$$

(3) If neither axis is significantly resolved, the best estimate for both the peak and integrated flux densities is the quantity

$$A^* \equiv A\left(\frac{\theta_{\rm M}\theta_{\rm m}}{\theta^2}\right)^{1/2} . \tag{42}$$

The rms uncertainty in A^* is

$$\sigma_{\rm A^*}^2 \approx \epsilon_{\rm A}^2 (A^*)^2 + \frac{(A^*)^2}{\rho^2} + \sigma_{\rm B}^2 \ . \tag{43}$$

To verify that the NVSS fluxes and their uncertainties have been estimated reliably, and to check on the completeness and reliability of the NVSS catalog at low flux densities, we cross-correlated it with sources stronger than 6σ in the deep 1412 MHz Westerbork/Einstein surveys 41W, 42W, 43W, and 44W (Katgert-Merkelijn *et al.* 1985). The resulting flux-flux diagram is shown in Figure 31. The scatter for most sources is consistent with NVSS catalog flux errors and (comparable) WSRT flux errors. A few percent of the sources lie well outside the 90% confidence limits in Figure 31. Such discrepancies could be caused by confusion in the large NVSS beam, resolution by the smaller WSRT beam, and source variability. NVSS catalog users should be aware that a small fraction of the flux densities will be in error by amounts much larger than the quoted uncertainties.

Noise and confusion limit the completeness of any catalog for faint sources. We define incremental completeness $C(S)$ to be the fraction of point sources with true flux densities near S which appear in the catalog. To measure $C(S)$, we added grids of artificial point sources to NVSS images and processed those images with our normal cataloging procedures. The points in Figure 32 show the fraction of the artificial sources cataloged as a function of true flux density (input flux density plus 0.3 mJy since the artificial sources have no clean bias). The smooth curve shows that these data are well fit by the integral of a Gaussian with mean 2.5 mJy and standard deviation 0.45 mJy, the rms fluctuation on most NVSS images. Thus the incremental completeness of the NVSS catalog for unresolved sources is 50% at 2.5 mJy and it rises rapidly to 99% at 3.4 mJy.

5.2.6. Linear Polarization

The Stokes Q and U brightnesses were obtained by interpolation at the total-intensity center position of each NVSS source. No fitting bias occurs because the noise on the Q and U images is independent of the noise on the I image. The clean bias correction was ignored as negligible because the polarized images contain few sources and are very lightly cleaned. However, the uncorrected estimate

$$L' = (Q^2 + U^2)^{1/2} \tag{44}$$

of the linearly polarized brightness is biased upward by image noise. If the rms noise in the Q and U images is $\sigma_{\rm Q,U}$, then the probability of estimating L' given a true linearly polarized brightness L is (Vinokur 1965)

$$P(L'|L) = \frac{L'}{\sigma^2_{\rm Q,U}} I_0\left(\frac{LL'}{\sigma^2_{\rm Q,U}}\right) \exp\left(-\frac{L^2 + L'^2}{2\sigma^2_{\rm Q,U}}\right) , \tag{45}$$

where I_0 is the modified Bessel function. The mean of L' given L

$$\langle L'|L\rangle = \int_0^\infty L' P(L'|L) dL' \tag{46}$$

is greater than L, so we subtract the polarization bias $\Delta L' \equiv \langle L'|L\rangle - L$. Introducing the normalized brightnesses $l' \equiv L'/\sigma_{\rm Q,U}$ and $l \equiv L/\sigma_{\rm Q,U}$ yields

$$\langle l'|l\rangle = \exp(-l^2/2) \int_0^\infty x^2 I_0(lx) \exp(-x^2/2) dx \tag{47}$$

which reduces to (Prudnikov *et al.* 1986)

$$\langle l'|l\rangle = (\pi/2)^{1/2} \exp(-l^2/2) M(3/2, 1, l^2/2) , \tag{48}$$

where M is the confluent hypergeometric function. For $l < 4$ we approximated M by the (slowly converging) power series in Jahnke & Emde (1945). For $l > 4$, we used the asymptotic expansion of M (Jahnke & Emde 1945): $\langle l'|l\rangle - l \approx (2l)^{-1} + (8l^3)^{-1}$.

The bias-corrected polarized brightness is listed by the fitted version of the NVSS catalog. Note that it can occasionally have (unphysical) negative estimated values. To approximate the bias-corrected polarized flux density of a slightly extended source, we simply multiplied the corrected polarized brightness by the ratio $\theta_{\rm M}\theta_{\rm m}/\theta^2$ of the total-intensity fitted area to the beam area. This quantity is given by the deconvolved version of the catalog. It may not be accurate for those very extended ($\theta_{\rm M} \gg \theta$) sources which have complex polarization structure on scales larger than the beam area.

The rms uncertainty in the corrected polarized brightness is

$$\sigma_{\rm P}^2 \approx 2\sigma_{\rm Q,U}^2 + \epsilon_{\rm P}^2 A_{\rm P}^2 \ , \tag{49}$$

where $\epsilon_{\rm P}$ is the residual instrumental polarization. If all strong sources were unpolarized, the distribution of their measured percentage polarizations would peak at $\epsilon_{\rm P}$. Thus the peak in the observed polarization distribution gives an upper limit to $\epsilon_{\rm P}$. We found $\epsilon_{\rm P} \approx 0.12\%$ for a large sample of sources stronger than 1 Jy. Since sources often have intrinsic polarizations larger than this, we cannot rule out the possibility that the instrumental polarization is occasionally much larger than $\epsilon_{\rm P}$. The rms uncertainty in the polarized flux density is $\sigma(L)(\theta_{\rm M}\theta_{\rm m}/\theta^2)$.

If the detection of polarized flux is significant at the 98% level, the polarization **E**-vector position angle PPA measured east from north is also given by both user versions of the NVSS catalog. The probability of measuring $l' > l_0$ with no polarized flux present is $\exp(-l_0^2/2)$, so our criterion for a significant detection is

$$L' > (2\ln 50)^{1/2}\sigma(L) \ . \tag{50}$$

The polarization position-angle distribution of significantly polarized sources is nearly Gaussian with rms uncertainty (deg)

$$\sigma(PPA) = \frac{90\sigma_{\rm Q,U}}{\pi(L' - \Delta L')} \ . \tag{51}$$

5.3. User Summary

The NVSS images now cover nearly all of the sky north of $\delta = -40^\circ$ at 1.4 GHz with $45''$ FWHM resolution in Stokes I (total intensity), Q, and U (linear polarization). The NVSS images, the catalog of sources on them, and user software are all available via Condon *et al.* (1998). Some examples of NVSS sources are shown in Figure 24 and discussed in Section 5.

The rms noise and confusion is $\sigma \approx 0.45$ mJy beam$^{-1} \approx 0.14$ K on the I images, except near strong sources. The dynamic range is 1000:1 locally and higher over scales greater than 30 arcmin. The Q and U images generally are noise limited with $\sigma \approx 0.29$ mJy beam$^{-1} \approx 0.09$ K, but the fluctuations are larger near the galactic plane. The images are insensitive to smooth radio structures much larger than several arcmin in both coordinates (diffuse synchrotron emission from the Galaxy and the 3 K cosmic microwave background, for example). Smooth sources somewhat larger than the one in the lower left panel of Figure 24 may be visible, but their image flux densities will probably be low. The image positions are known to be slightly offset ($\langle \Delta\alpha \rangle = +0\farcs025 \pm 0\farcs022$ and $\langle \Delta\delta \rangle = -0\farcs113 \pm 0\farcs027$), and clean bias (Section 4.1) depresses the peak flux densities of most sources by about $\Delta S_{\rm P} = -0.3$ mJy beam^{-1} on the images.

The NVSS "source" catalog lists all discrete image peaks with uncorrected brightness $S_{\rm P} \geq 2$ mJy beam^{-1}. Extended radio sources may be represented by two or more fitted peaks. There are two user versions of the NVSS catalog, both of which list positions and flux densities corrected for known biases. The "fitted" version returns peak flux densities and fitted sizes; the "deconvolved" version returns integrated flux densities and estimates of source sizes after the point-source response has been deconvolved from the fits. The rms uncertainties of these parameters are generally well determined, but occasionally the flux-density errors will be much larger (low flux densities of very extended sources, high flux densities of confused sources). The incremental completeness (defined in Section 5.2.5) of the NVSS catalog is 50% for unresolved sources with corrected flux density $S = 2.5$ mJy and rises rapidly to 99% at 3.4 mJy (Figure 32).

To avoid ambiguity, please refer to NVSS catalog sources by their full IAU designations (Lortet *et al.* 1994) of the form: `NVSS JHHMMSS+DDMMSS`, where `NVSS` is the catalog acronym, `J` specifies the coordinate equinox (either `J` for J2000 or `B` for B1950), `HHMMSS` are the hours, minutes, and truncated (not rounded) seconds of right ascension, `+` or `-` is the sign of the declination, and `DDMMSS` are the degrees, arc minutes, and truncated (not rounded) arc seconds of declination. Thus the NVSS source at J2000 $\alpha = 00^{\rm h}00^{\rm m}00\fs24$, $\delta = -20^\circ04'49\farcs1$ (= B1950 $\alpha = 23^{\rm h}57^{\rm m}26\fs34$, $\delta = -20^\circ21'31\farcs4$) is called NVSS J000000−200449 or NVSS B235726−202131.

We thank Frazer Owen and the survey oversight committee for helpful guidance. This research was supported in part by NSF Grant No. AST-9320547. The Digitized Sky Surveys were produced at the Space Telescope Science Institute under U.S. Government grant NAG W-2166. This research has made use of the NASA/IPAC Extragalactic Database (NED) which is operated by the Jet Propulsion Laboratory, California Institute of Technology, under contract with the National Aeronautics and Space Administration.

Table 1. Survey Declination Bands

Band	Grid Row Numbers	Declination Range (J2000)	Grid Columns	Config-uration	Snapshot Duration
1	532—509	$-40^\circ\ 10'\ 24'' \leq \delta \leq -34^\circ\ 22'\ 54''$	960	DnC	60 s
2	508—475	$-34^\circ\ 08'\ 12'' \leq \delta \leq -26^\circ\ 18'\ 48''$	960	DnC	50 s
3	474—403	$-26^\circ\ 05'\ 00'' \leq \delta \leq -10^\circ\ 14'\ 12''$	960	DnC	40 s
4	402—275	$-10^\circ\ 01'\ 00'' \leq \delta \leq +17^\circ\ 44'\ 18''$	960	D	30 s
5	274—243	$+17^\circ\ 57'\ 36'' \leq \delta \leq +24^\circ\ 56'\ 12''$	960	D	30 s
6	242—166	$+25^\circ\ 09'\ 54'' \leq \delta \leq +43^\circ\ 54'\ 42''$	960	D	30 s
7	165—122	$+44^\circ\ 11'\ 18'' \leq \delta \leq +58^\circ\ 15'\ 30''$	960	D	30 s
8	121—058	$+58^\circ\ 27'\ 36'' \leq \delta \leq +74^\circ\ 47'\ 24''$	480	D	30 s
9	057—044	$+74^\circ\ 59'\ 30'' \leq \delta \leq +77^\circ\ 52'\ 24''$	240	D	30 s
10	043—028	$+78^\circ\ 06'\ 54'' \leq \delta \leq +82^\circ\ 31'\ 06''$	240	DnC	40 s
11	027—012	$+82^\circ\ 43'\ 24'' \leq \delta \leq +86^\circ\ 44'\ 42''$	120	DnC	40 s
12	011—006	$+86^\circ\ 58'\ 24'' \leq \delta \leq +88^\circ\ 21'\ 18''$	60	DnC	40 s
13	005—002	$+88^\circ\ 34'\ 54'' \leq \delta \leq +89^\circ\ 24'\ 48''$	30	DnC	40 s
14	001—000	$+89^\circ\ 42'\ 24'' \leq \delta \leq +90^\circ\ 00'\ 00''$	(6)	DnC	40 s

Table 2. NVSS $4^\circ \times 4^\circ$ Image Centers

$\|\delta_0\|$ (deg)	α_0	Number/row
0, 4, …, 28	$0^{\rm m}$, $16^{\rm m}$, $32^{\rm m}$, …, $23^{\rm h}\ 44^{\rm m}$	90
32, 36	$0^{\rm m}$, $18^{\rm m}$, $36^{\rm m}$, …, $23^{\rm h}\ 42^{\rm m}$	80
40, 44, 48	$0^{\rm m}$, $20^{\rm m}$, $40^{\rm m}$, …, $23^{\rm h}\ 40^{\rm m}$	72
52, 56	$0^{\rm m}$, $24^{\rm m}$, $48^{\rm m}$, …, $23^{\rm h}\ 36^{\rm m}$	60
60, 64	$0^{\rm m}$, $30^{\rm m}$, $1^{\rm h}$, …, $23^{\rm h}\ 30^{\rm m}$	48
68	$0^{\rm m}$, $36^{\rm m}$, $1^{\rm h}\ 12^{\rm m}$, …, $23^{\rm h}\ 24^{\rm m}$	40
72, 76	$0^{\rm m}$, $45^{\rm m}$, $1^{\rm h}\ 30^{\rm m}$, …, $23^{\rm h}\ 15^{\rm m}$	32
80	$0^{\rm h}$, $1^{\rm h}$, $2^{\rm h}$, …, $23^{\rm h}$	24
84	$0^{\rm h}$, $1^{\rm h}\ 30^{\rm m}$, $3^{\rm h}$, …, $22^{\rm h}\ 30^{\rm m}$	16
88	$0^{\rm h}$, $3^{\rm h}$, $6^{\rm h}$, …, $21^{\rm h}$	8

REFERENCES

Baars, J. W. M., Genzel, R., Pauliny-Toth, I. I. K., & Witzel, A. 1977, A&A, 61, 99

Bahcall, J. N., & Soneira, R. M. 1980, ApJS, 44, 73

Bahcall, J. N., & Soneira, R. M. 1981, ApJS, 47, 357

Baldwin, J. E., Boysen, R. C., Hales, S. E. G., Jennings, J. E., Waggett, P. C., Warner, P. J., & Wilson, D. M. A. 1985, MNRAS, 217, 717

Ball, J. A. 1975, in Methods of Computational Physics, edited by B. Alder, S. Fernbach, and M. Rotenberg (Academic, New York), Vol. 14, p. 177

Becker, R. H., White, R. L., & Edwards, A. L. 1991, ApJS, 75, 1

Becker, R. H., White, R. L., & Helfand, D. J. 1995, ApJ, 450, 559

Chu, T. S., & Turrin, R. H. 1973, IEEE Trans. Ant. Prop., AP-21, 339

Condon, J. J. 1974, ApJ, 188, 279

Condon, J. J. 1984, ApJ, 287, 461

Condon, J. J. 1992, ARA&A, 30, 575

Condon, J. J. 1997, PASP, 109, 166

Condon, J. J., Anderson, M. A., & Helou, G. 1991a, ApJ, 376, 95

Condon, J. J., Balonek, T. J., & Jauncey, D. L. 1975, AJ, 80, 887

Condon, J. J., & Broderick, J. J. 1986, AJ, 92, 94

Condon, J. J., Cotton, W. D., Greisen, E. W., Yin, Q. F., Perley, R. A., Taylor, G. B., & Broderick, J. J. 1998, NVSS web site in `http://www.nrao.edu`

Condon, J. J., Frayer, D. T., & Broderick, J. J. 1991b, AJ, 101, 362

Condon, J. J., Huang, Z.-P., Yin, Q. F., & Thuan, T. X. 1991c, ApJ, 378, 65

Cornwell, T., & Braun, R. 1989, in Synthesis Imaging in Radio Astronomy, edited by R. A. Perley, F. R. Schwab, & A. H. Bridle (ASP, San Francisco), p. 167

Cotton, W. D. 1994, AIPS Memo 86 (NRAO, Charlottesville)

Cotton, W. D., Tody, D., & Pence, W. D. 1995, A&AS, 112, 159

Cox, M. J., Eales, S. A. E., Alexander, P., & Fitt, A. J. 1988, MNRAS, 235, 1227

Crane, P. C., & Napier, P. J. 1989, in Synthesis Imaging in Radio Astronomy, edited by R. A. Perley, F. R. Schwab, & A. H. Bridle (ASP, San Francisco), p. 139

de Bruyn, A. G. 1977, A&A, 54, 491

de Bruyn, G., Miley, G., Tang, Y., Bremer, M., Brouw, W., Rengelink, R., Bremer, M., & Röttgering, H. 1994, ASTRON/NFRA newsletter Aug. 1994, 4

Green, A. J. 1997, PubASA, 14, 73

Gregory, P. C., Vavasour, J. D., Scott, W. K., & Condon, J. J. 1994, ApJS, 90, 173

Greisen, E. W. 1983, AIPS Memo 27 (NRAO, Charlottesville)

Griffith, M., Wright, A. E., Burke, B. F., & Ekers, R. D. 1994, ApJS, 90, 179

Griffith, M., Wright, A. E., Burke, B. F., & Ekers, R. D. 1995, ApJS, 97, 347

Hartwick, F. D. A., & Schade, D. 1990. ARA&A, 28, 437

Jahnke, E., & Emde, F. 1945, Tables of Functions (Dover, New York), p. 275

Johnston, K. J. *et al.* 1995, AJ, 110, 880

Katgert-Merkelijn, J. K., Robertson, J. G., Windhorst, R. A., & Katgert, P. 1985, A&AS, 61, 517

Lortet, M.-C., Borde, S., Ochsenbein, F. 1994, A&AS, 107, 193

McGilchrist, M. M., Baldwin, J. E., Riley, J. M., Titterington, D. J., Waldram, E. M., & Warner, P. J. 1990, MNRAS, 246, 110

Mitchell, K. J., & Condon, J. J. 1985, AJ, 90, 1957

Moshir, M. *et al.* 1992, Explanatory Supplement to the *IRAS* Faint Source Survey, Version 2, JPL D-10015 8/92 (Jet Propulsion Laboratory, Pasadena)

Nilson, P. 1973, Uppsala General Catalog of Galaxies (Uppsala Astronomical Observatory, Uppsala)

Perley, R. A. 1989, in Synthesis Imaging in Radio Astronomy, edited by R. A. Perley, F. R. Schwab, & A. H. Bridle (ASP, San Francisco), p. 259

Peterson, B. A., Ellis, R. A., Kibblewhite, E. J., Bridgeland, M. T., Hooley, T., & Horne, D. 1979, ApJ, 233, L109

Prudnikov, A. P., Brychkov, Yu. A., & Marichev, O. I. 1986, Integrals and Series, Vol. 2 (Gordon & Breach, New York), p. 306

Rengelink, R. B., Tang, Y., de Bruyn, A. G., Miley, G. K., Bremer, M. N., Röttgering, H. J. A., & Bremer, M. A. R. 1997, A&S, 124, 259

Rowan-Robinson *et al.* 1991, Nature, 351, 719

Sanders, D. B., Soifer, B. T., Elias, J. H., Madore, B. F., Matthews, K., Neugebauer, G., & Scoville, N. Z. 1988, ApJ, 325, 74

Simard-Normandin, M., Kronberg, P. P., & Button, S. 1981, ApJS, 45, 97

Spangler, S. R., & Cotton, W. D. 1981, AJ, 86, 730

Sramek, R. A., & Schwab, F. R. 1989, in Synthesis Imaging in Radio Astronomy, edited by R. A. Perley, F. R. Schwab, & A. H. Bridle (ASP, San Francisco), p. 117

Vinokur, M. 1965, AnnAp, 28, 412

Voges, W. *et al.* 1997, A&A, in press

White, R. L., Becker, R. H., Helfand, D. J., & Gregg, M. D. 1997, Astrophysical Journal, 475, 479

Windhorst, R. A., Kron, R. G., & Koo, D. C. 1984, A&AS, 58, 39

Windhorst, R. A., Mathis, D. F., & Neuschaefer, L. W. 1990, in Evolution of the Universe of Galaxies, edited by R. Kron (ASP, San Francisco), p. 389

Wright, A. E., & Otrupcek, R. E. 1990, PKSCAT90 Radio Source Catalogue and Sky Atlas (Australia Telescope National Facility, Parkes)

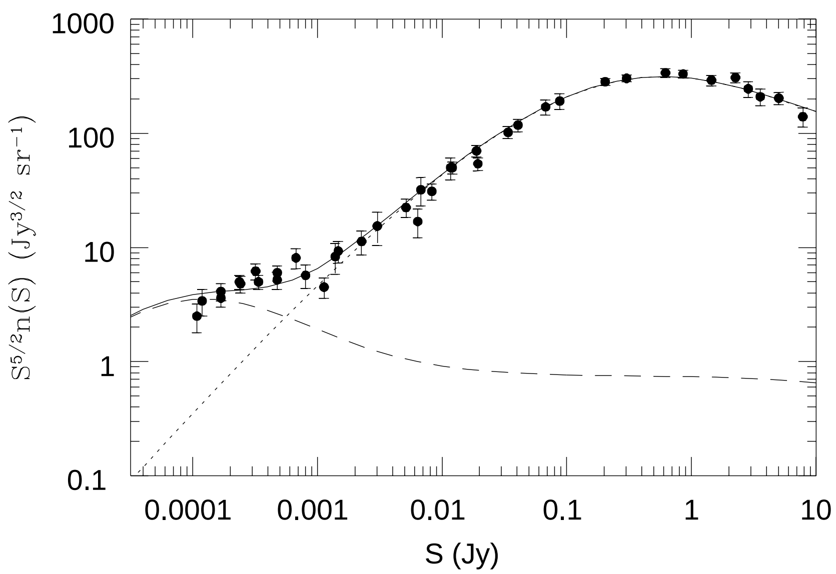

Fig. 1.— Weighted source counts at 1.4 GHz (data points) and models (Condon 1984) indicating the contributions of evolving "monsters" in powerful AGN (dotted curve) and normal galaxies plus "starbursts" and low-luminosity AGN (e.g., Seyfert galaxies) (dashed curve) to the total (continuous curve). The quantity $n(S)\ ds$ is the number of sources per steradian with flux densities between S and $S + dS$, and weighting by $S^{5/2}$ divides by the counts expected in a static Euclidean universe. Abscissa: flux density (Jy). Ordinate: weighted source density ($\mathrm{Jy}^{3/2}$ sr^{-1}.)

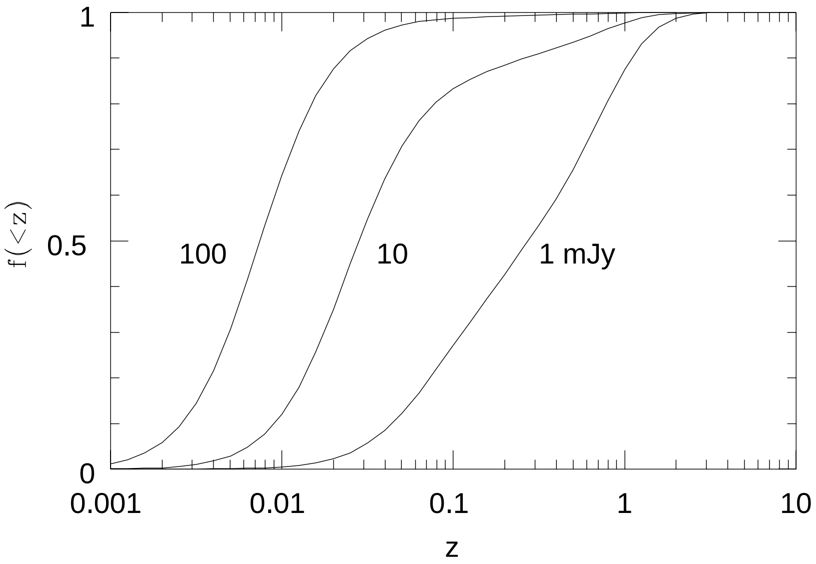

Fig. 2.— The cumulative fraction $f(< z)$ of radio sources with redshifts $< z$ that are powered by stars changes dramatically as the 1.4 GHz flux density falls from 100 mJy through 10 mJy to 1 mJy. These curves are based on the evolutionary model in Condon (1984). Abscissa: redshift z. Ordinate: fraction of sources with redshift $< z$.

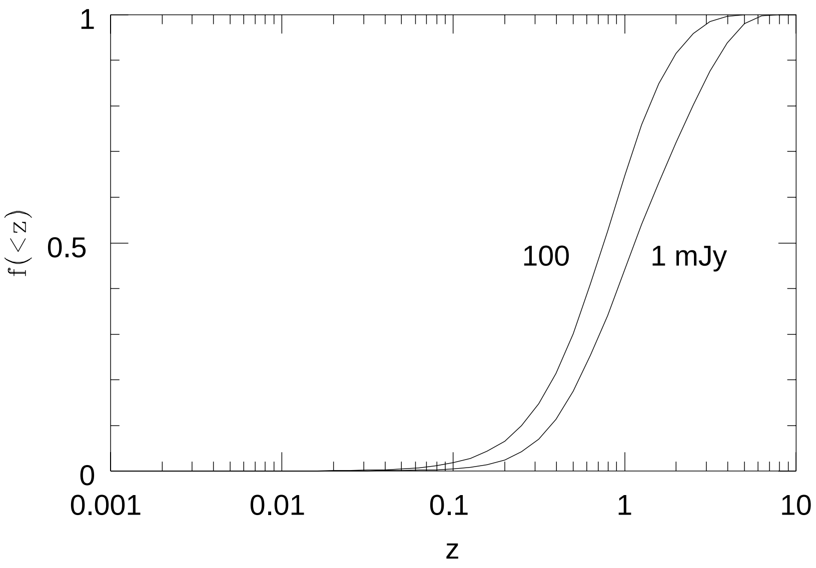

Fig. 3.— The cumulative fraction $f(< z)$ of radio AGN with redshifts $< z$ is nearly independent of 1.4 GHz flux density between 100 mJy and 1 mJy. These curves are based on the evolutionary model in Condon (1984). Abscissa: redshift z. Ordinate: fraction of sources with redshift $< z$.

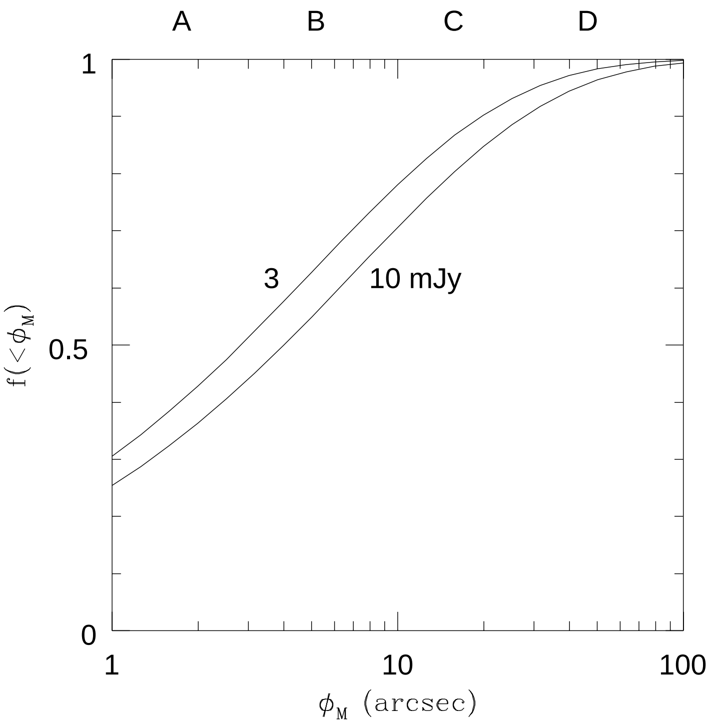

Fig. 4.— The cumulative fraction $f(< \phi_{\rm M})$ of radio sources with largest angular size $\phi_{\rm M}$ at 1.4 GHz flux densities $S = 3$ and 10 mJy. Typical VLA A-, B-, C-, and D-configuration resolutions at 1.4 GHz are indicated above the plot. Abscissa: largest angular size $\phi_{\rm M}$ (arcsec). Ordinate: fraction of sources smaller than $\phi_{\rm M}$.

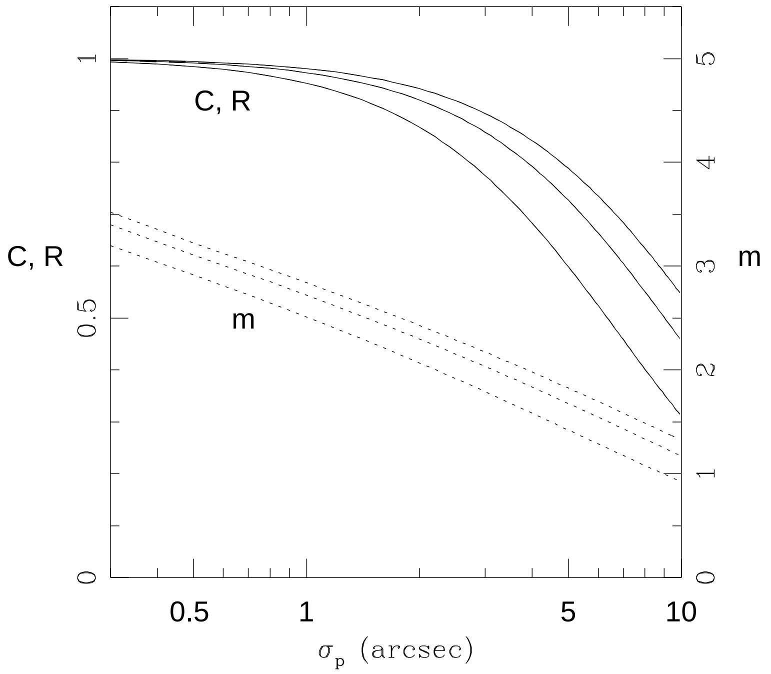

Fig. 5.— The normalized radius $m \equiv r_{\rm s}/\sigma_{\rm p}$ of the identification search circle can be varied with the rms position uncertainty $\sigma_{\rm p}$ to keep the identification completeness C approximately equal to the identification reliability R. The three continuous curves for $C = R$ and the three broken curves for m correspond to unrestricted position-coincidence identifications of faint radio sources with optical objects brighter than $J = 22.5$ (true identification rate $f \approx 0.3$) near the galactic pole (top), at $|b| = 30°$, $|l| = 90°$ (middle), and in the galactic bulge $|b| \lesssim 30°$, $|l| \lesssim 45°$ (bottom). Abscissa: rms position error in each coordinate (arcsec). Left ordinate: identification completeness C and reliability R. Right ordinate: ratio m of search radius to rms position error (dimensionless) that results in $C \approx R$.

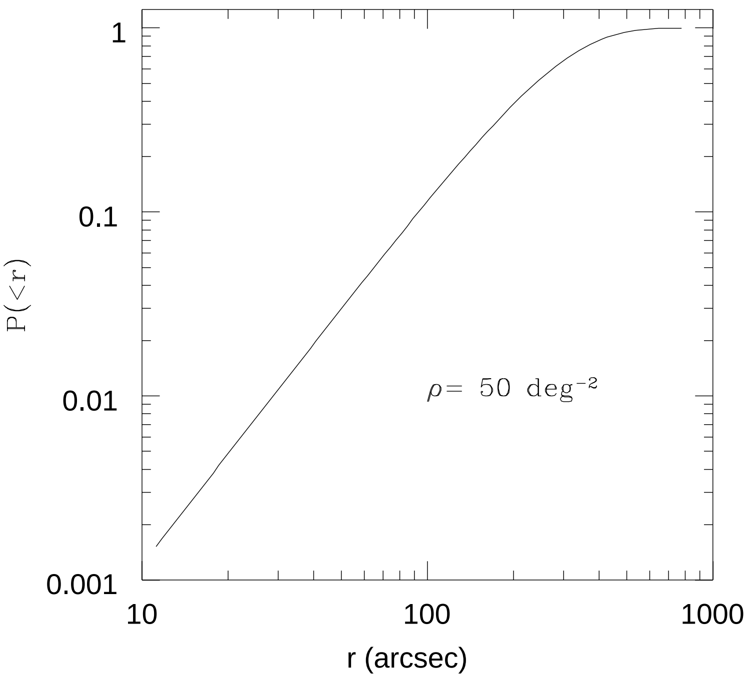

Fig. 6.— The probability $P(< r)$ of finding an unrelated radio source within angular distance r of an arbitrary input position, for the NVSS source density $\rho \approx 50$ deg^{-2}. Abscissa: distance to nearest source (arcsec). Ordinate: probability of finding an unrelated source (dimensionless).

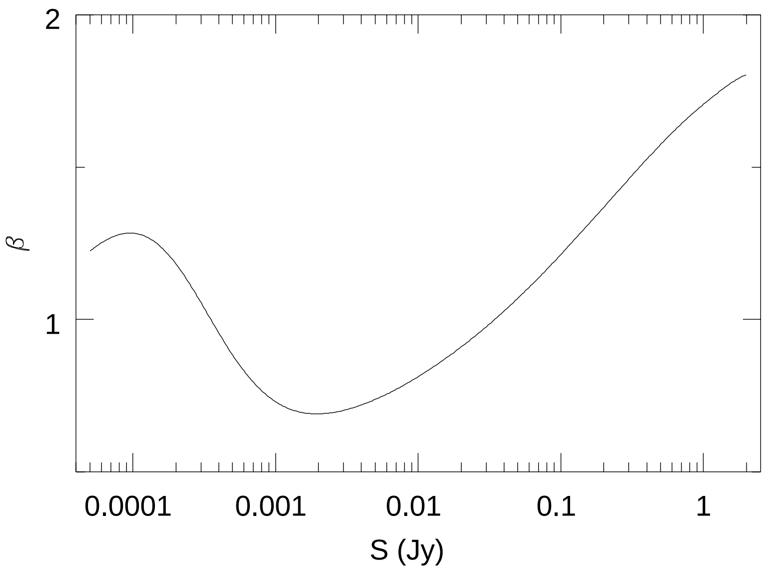

Fig. 7.— The logarithmic slope of the cumulative source count has a minimum $\beta \approx 0.7$ near $S = 2$ mJy at 1.4 GHz. Abscissa: flux density at 1.4 GHz (Jy). Ordinate: logarithmic slope of cumulative source count (dimensionless).

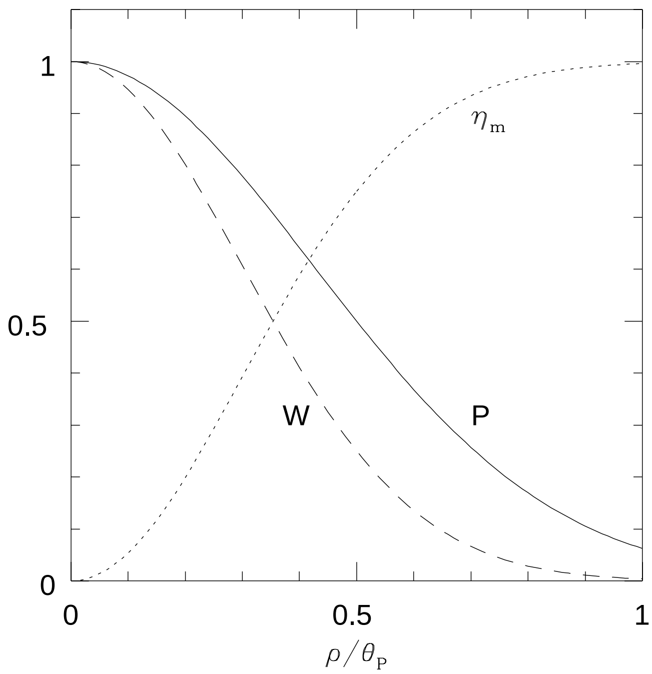

Fig. 8.— The normalized primary-beam power pattern P, the weight beam W, and the mapping efficiency $\eta_{\rm m}$ are shown for a Gaussian primary beam with FWHM $\theta_{\rm P}$. Abscissa: distance from the pointing center, in units of the primary FWHM. Ordinate: P, W, or $\eta_{\rm m}$ (all dimensionless).

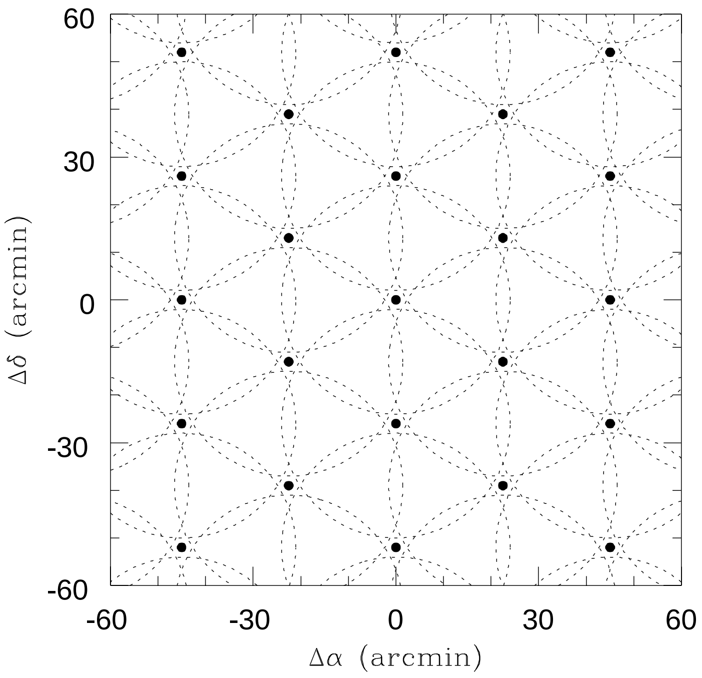

Fig. 9.— The VLA can cover the sky uniformly and efficiently with 1.4 GHz snapshot images whose pointing centers (filled circles) lie on a hexagonal grid with separation $\Delta = 26'$. The $\rho_{\rm m} = 24'$ image boundaries are indicated by dotted circles. Abscissa: right ascension offset (arcmin). Ordinate: declination offset (arcmin).

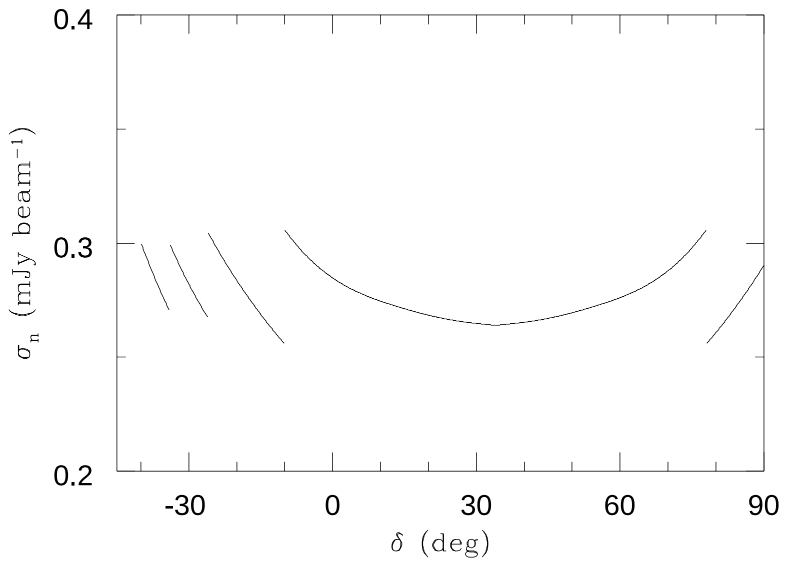

Fig. 10.— The theoretical rms noise level at the center of an NVSS snapshot image varies little with declination because the integration times increase from 30 s ($-10^\circ < \delta < -78^\circ$) to 40, 50, and 60 s at higher zenith angles. Abscissa: declination (degrees). Ordinate: theoretical rms noise (mJy beam^{-1}).

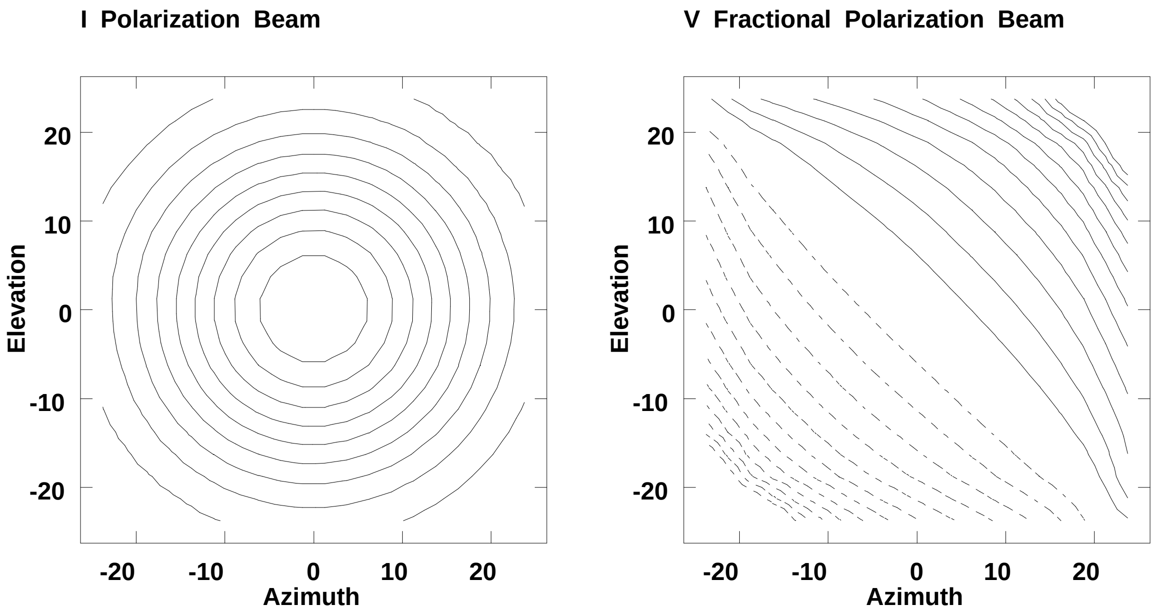

Fig. 11.— The total-intensity beam is nearly circular, even though it is the average of two offset circular-polarization beams and the fractional circular polarization caused by beam squint is large. Abscissae: azimuth offset (arcmin). Ordinates: elevation offset (arcmin). Contour levels: 0.1, 0.2, ... 0.9 (I polarization); ±0.02, ±0.04, ..., ±0.22 (V fractional polarization).

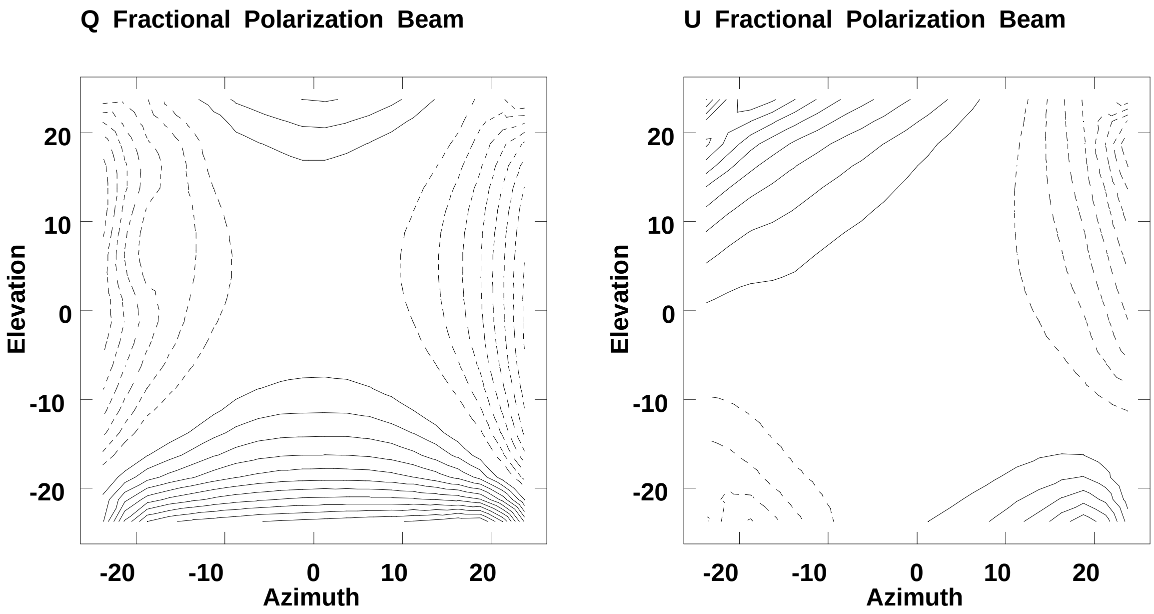

Fig. 12.— Although the VLA Q and U fractional polarizations are large far from the telescope axis, they are well defined and depend only on the azimuth and elevation offsets. Abscissae: azimuth offset (arcmin). Ordinates: elevation offset (arcmin). Contour levels: ± 0.01, ± 0.02, ± 0.03,...

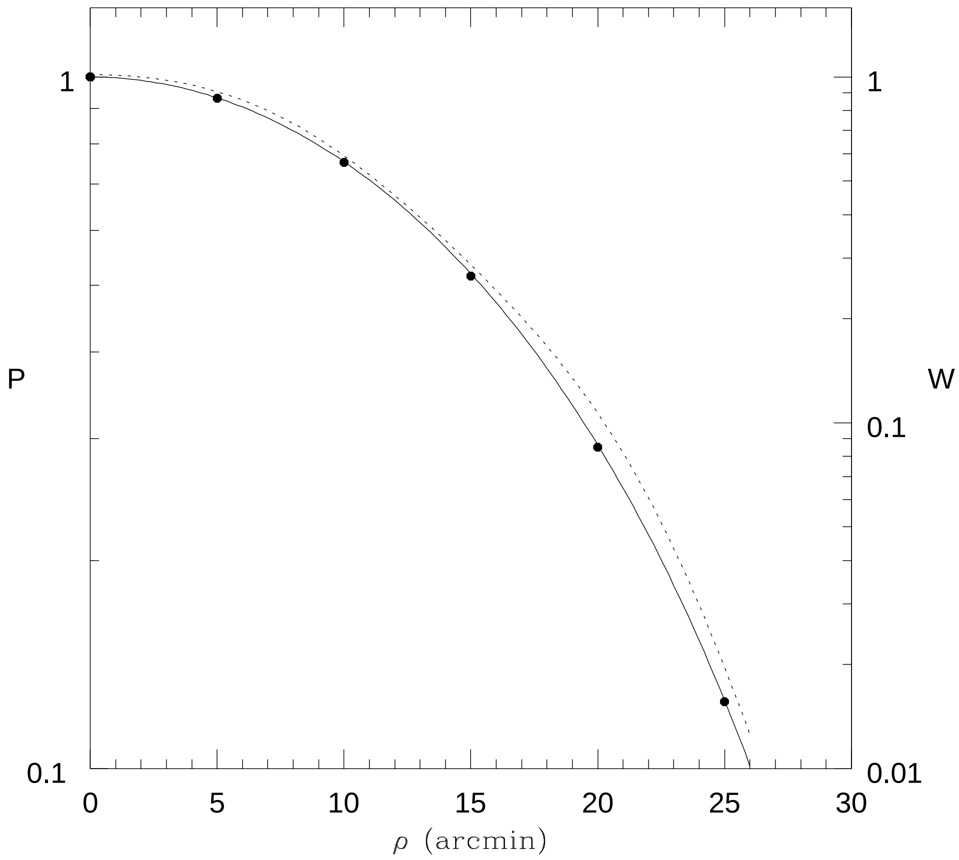

Fig. 13.— The 1.4 GHz primary power pattern P is nearly circular. Its observed radial profile (filled circles) is well fit by the theoretical pattern of a uniformly illuminated circular aperture 24.5 m in diameter (continuous curve). It is slightly narrower than the "standard" profile used by the AIPS task PBCOR (dotted curve). Abscissa: angular distance from the pointing center (arcmin). Left ordinate: relative power. Right ordinate: statistical weight $W \propto P^2$.

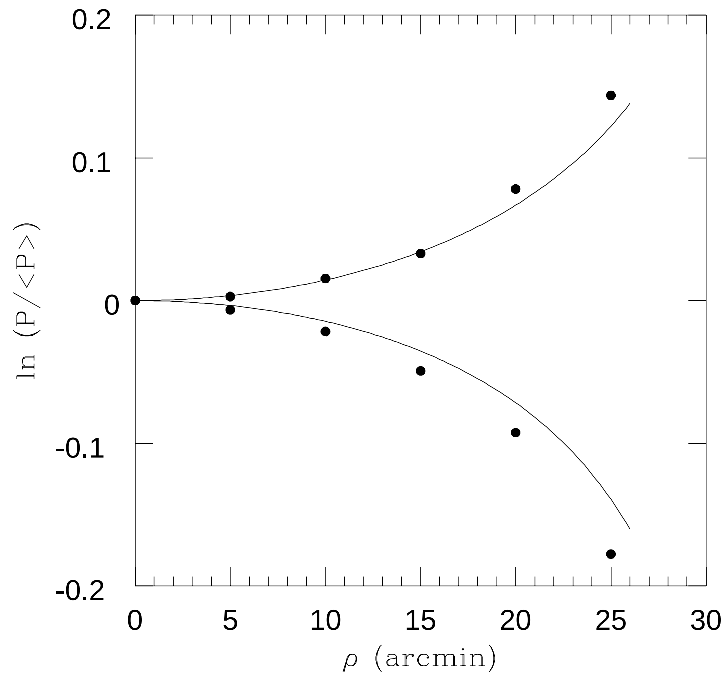

Fig. 14.— The primary beamwidth scales roughly as ν^{-1} so the intensity P of a point source, relative to the average $\langle P \rangle$ of both IFs, is significantly higher in the 1364.9 MHz IF channel (upper curve) than in the 1435.1 MHz IF channel (lower curve) at large angular distances ρ from the pointing center. The measured data are shown as filled circles. The calculated curves are for a uniformly illuminated 24.5 m circular aperture whose beamwidth is proportional to ν^{-1}. Abscissa: angular distance from the pointing center (arcmin). Ordinate: natural log of power in one IF channel relative to the average power in both IF channels.

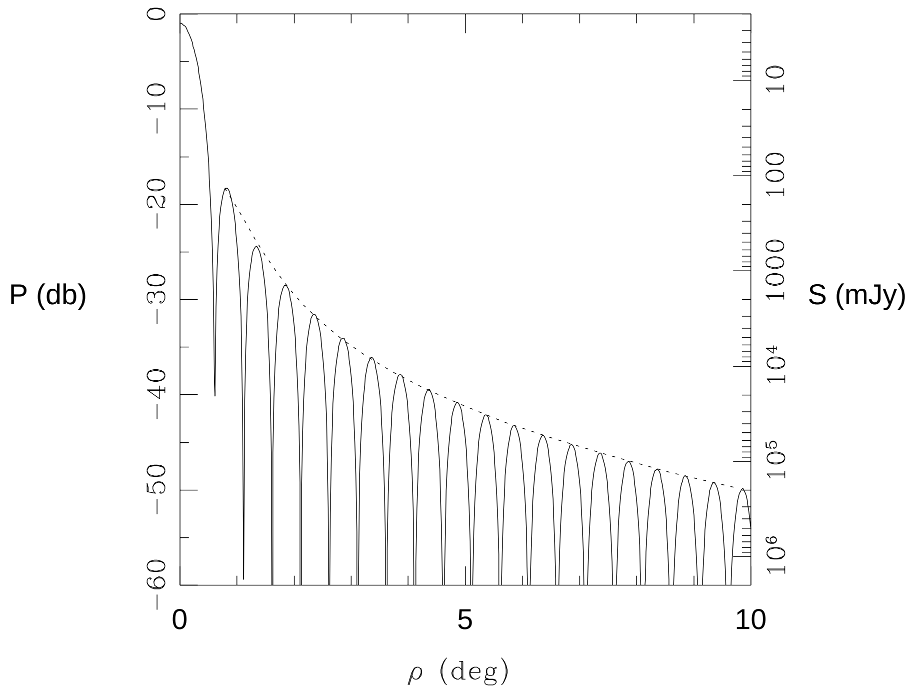

Fig. 15.— The upper envelope (dotted curve) of the theoretical power pattern of a 24.5 m circular aperture at $\nu = 1.4$ GHz (continuous curve) was used to determine the maximum angular distance ρ at which a source of flux density S could have an apparent flux density ≥ 2 mJy. Such sources must be imaged and cleaned separately. Abscissa: angular distance from the pointing center (deg). Left ordinate: primary beam attenuation (decibels). Right ordinate: minimum flux density of a source requiring separate imaging (mJy).

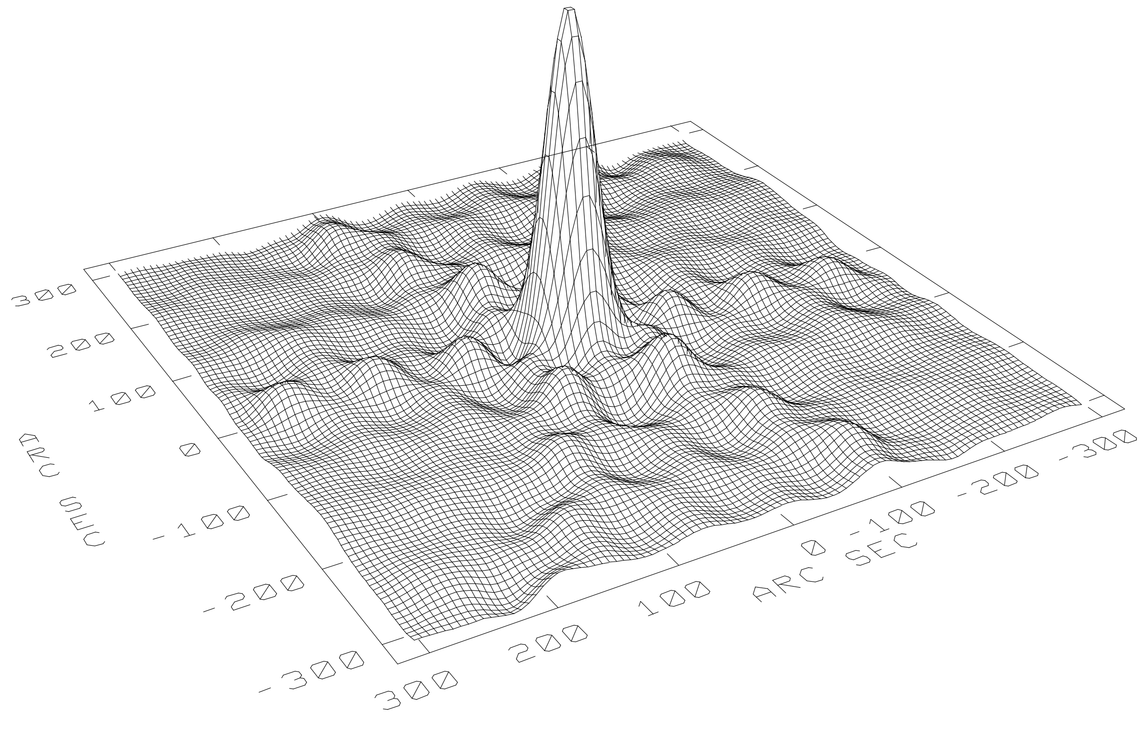

Fig. 16.— With super-uniform weighting, the synthesized beam has a nearly Gaussian main lobe whose FWHM is about 45″. The nearby sidelobes are fairly small and have nearly zero mean. Abscissa: right-ascension offset (arcsec). Ordinate: declination offset (arcsec).

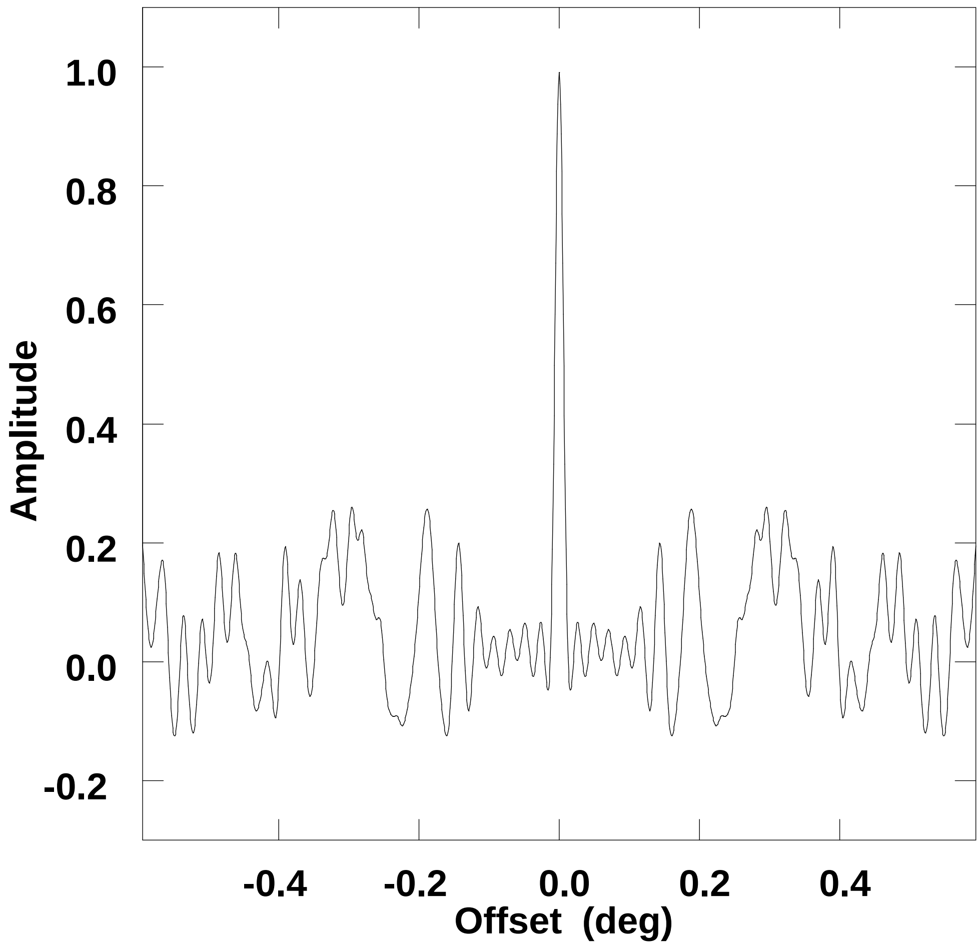

Fig. 17.— By far the largest sidelobes of the synthesized beam lie along three narrow diffraction spikes normal to the VLA arms. The broad peaks near ± 0.3 deg offset are grating lobes corresponding to the shortest projected spacings, about 37 m $\approx 170\lambda$. Abscissa: offset from beam center (deg). Ordinate: relative power (dimensionless).

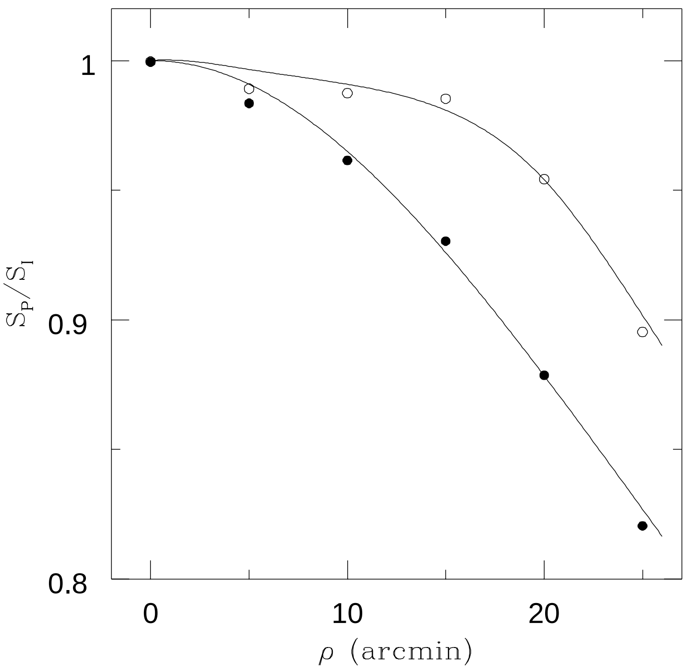

Fig. 18.— Bandwidth smearing reduces the peak flux density $S_{\rm P}$ of a point source but preserves the integrated flux density $S_{\rm I}$. The observed reduction of $S_{\rm P}/S_{\rm I}$ with angular distance ρ from the phase center is shown with (open circles) and without (filled circles) the bandwidth-smearing correction. Abscissa: angular distance from the phase center (arcmin). Ordinate: ratio of peak to integrated flux density (dimensionless).

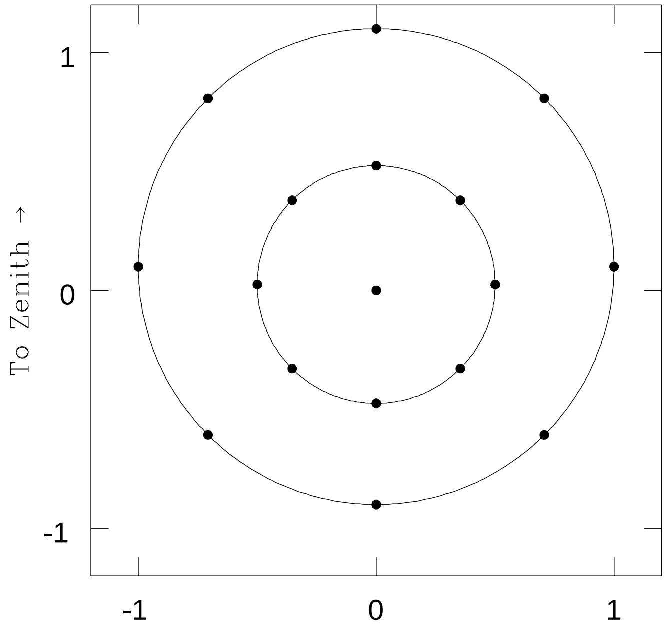

Fig. 19.— The image made from a two-dimensional Fourier transform of snapshot data taken by an instantaneously coplanar array is distorted as shown above. The sources should lie on straight lines and on circles concentric with the origin and having radii 0.5 and 1.0. Abscissa: azimuth offset (arbitrary units). Ordinate: zenith offset (arbitrary units).

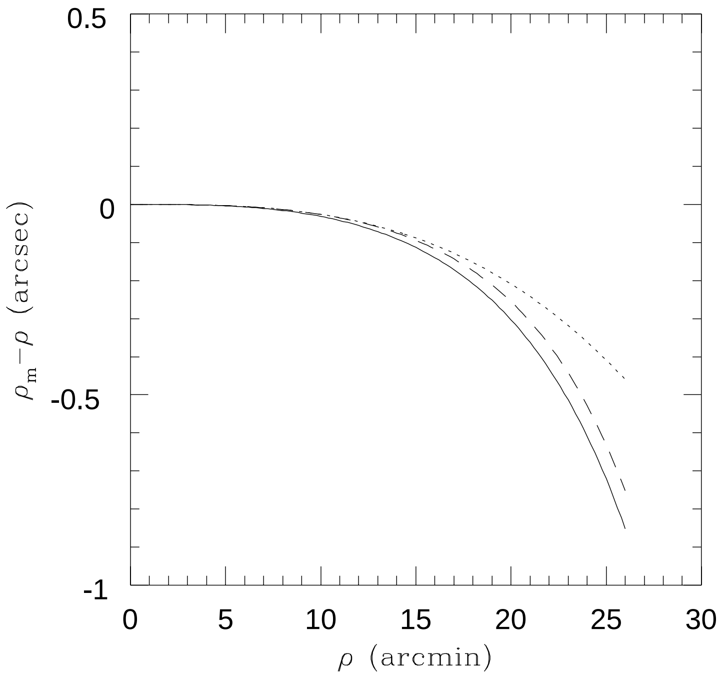

Fig. 20.— A source at angular distance ρ from the pointing center will appear at angular distance $\rho_{\rm m} \lesssim \rho$ because the effective centroid frequency is lowered by the frequency dependence of the primary beamwidth. The dotted line was calculated for a Gaussian primary beam with FWHM $\theta_{\rm P} = 30\farcm83$, the dashed line for the beam of a uniformly illuminated circular aperture. The solid curve is a cubic fit based on the measured values of $\partial \ln P/\partial\nu$. Abscissa: true angular distance from the center (arcmin). Ordinate: error in image angular distance from the center (arcsec).

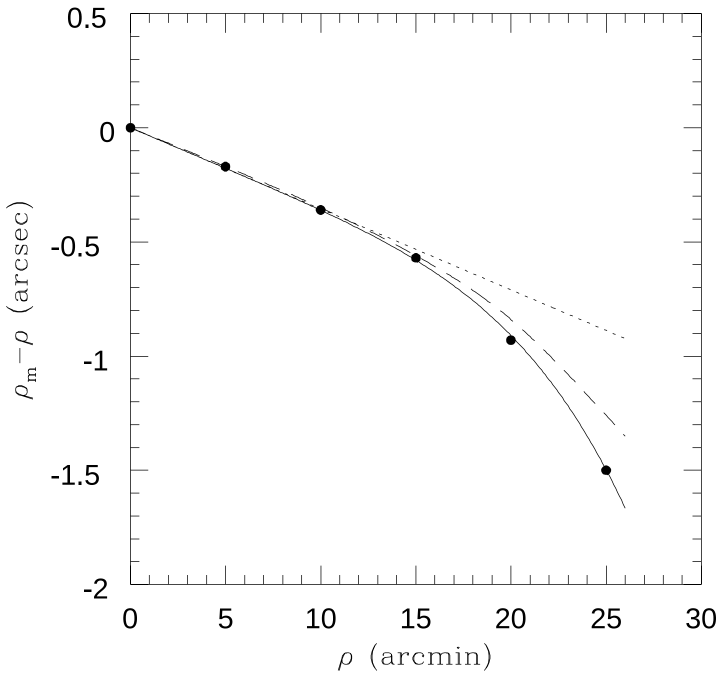

Fig. 21.— Multiplication of the snapshot image by the primary power pattern moves the centroid of a point source toward the image center. The resulting shift ($\rho_{\rm m} - \rho$) in centroid distance from the image center must be corrected. The dotted line shows the calculated shift for a Gaussian primary beam, the dashed line for the primary beam of a uniformly illuminated circular aperture. A smooth fit (continuous curve) to the measured values (filled circles) was used to make the correction. Abscissa: true angular distance from the center (arcmin). Ordinate: error in image angular distance from the center (arcsec).

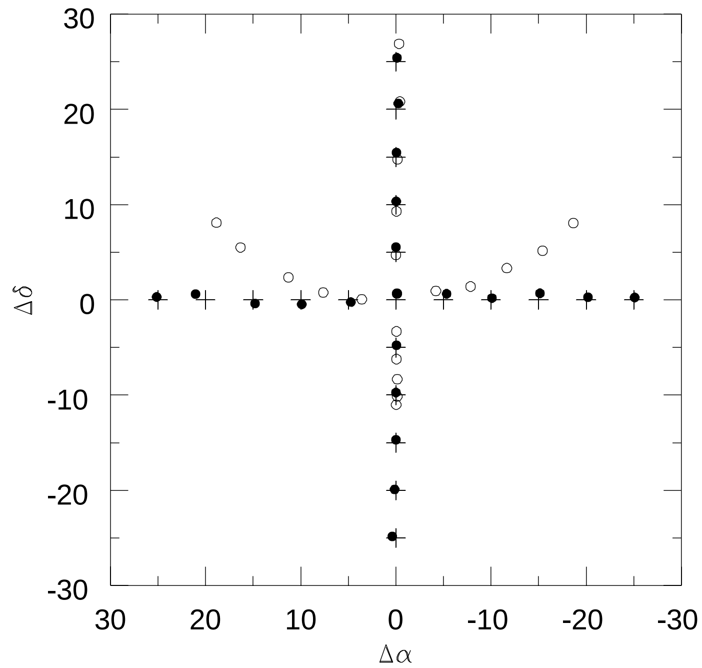

Fig. 22.— The true position offsets (arcmin) were added to their errors (arcsec) before (open circles) and after (filled circles) the geometric corrections were applied to transit observations of the southern source J1833−210 ($Z \approx 55°$, $\chi \approx 180°$). Abscissa: right-ascension position offset (arcmin) or error (arcsec). Ordinate: declination position offset (arcmin) or error (arcsec).

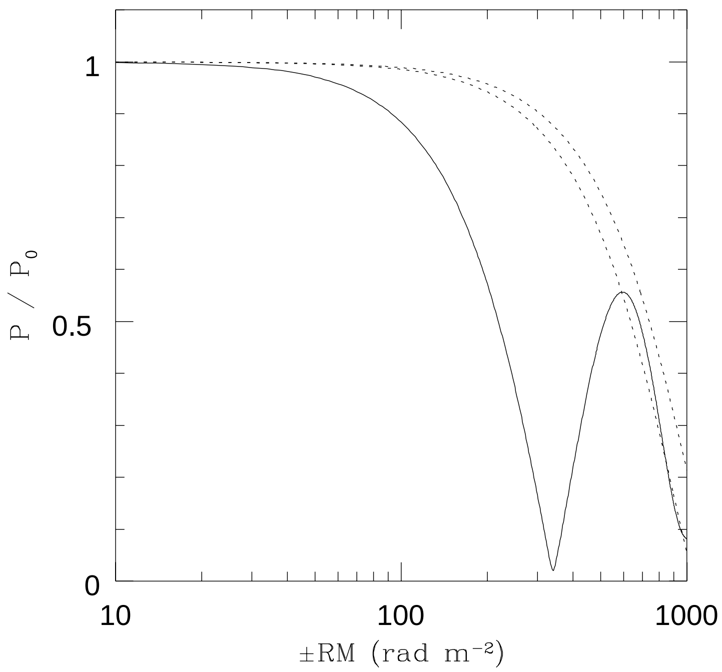

Fig. 23.— Differential Faraday rotation within and between the two wide IF passbands reduces the linearly polarized brightness in the NVSS images. The left and right broken curves indicate the ratios of image polarized brightness P to the polarized brightness P_0 in a very narrow band, for images made with $\Delta\nu = 42$ MHz bandwidth centered at $\nu = 1364.9$ MHz and $\nu = 1435.1$ MHz, respectively. Normal NVSS images made from both IF channels have polarization ratios shown by the continuous curve. Abscissa: absolute value of rotation measure (rad m^{-2}). Ordinate: ratio of image to true polarization brightness.

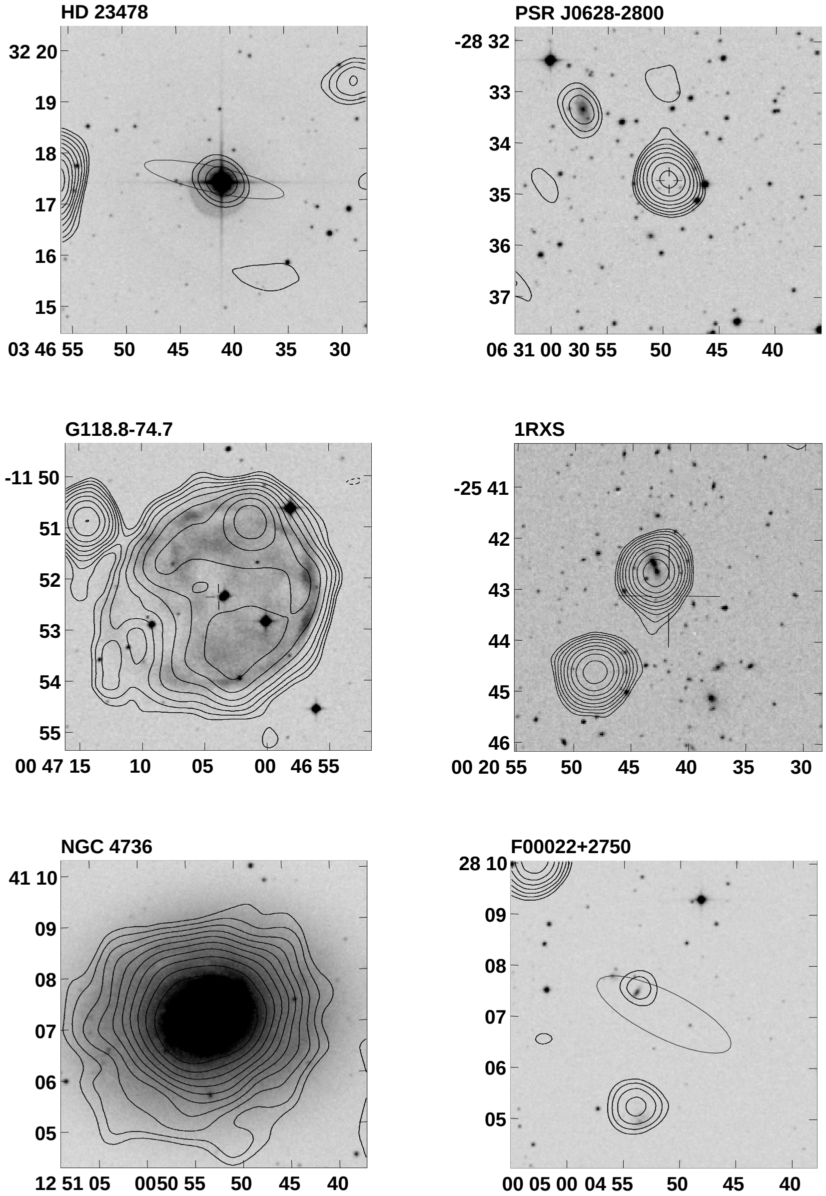

Fig. 24.— Six postage-stamp images showing the NVSS (contours) over Digitized Sky Survey optical images (gray scale). The contours are plotted at 1 mJy beam^{-1} $\times$ $\pm 2^0$, $\pm 2^{1/2}$, $\pm 2^1$, $\pm 2^{3/2}$.... Abscissae: J2000 right ascension. Ordinates: J2000 declination.

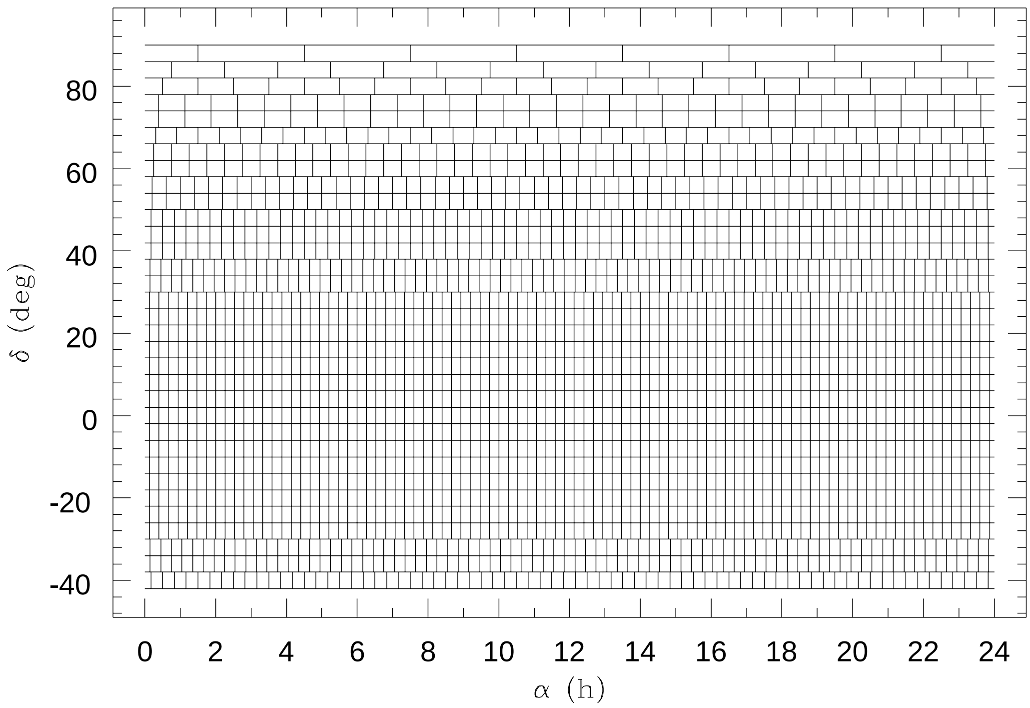

Fig. 25.— Boundaries of the 2326 $4^\circ \times 4^\circ$ NVSS sky images. Abscissa: J2000 right ascension (h). Ordinate: J2000 declination (deg).

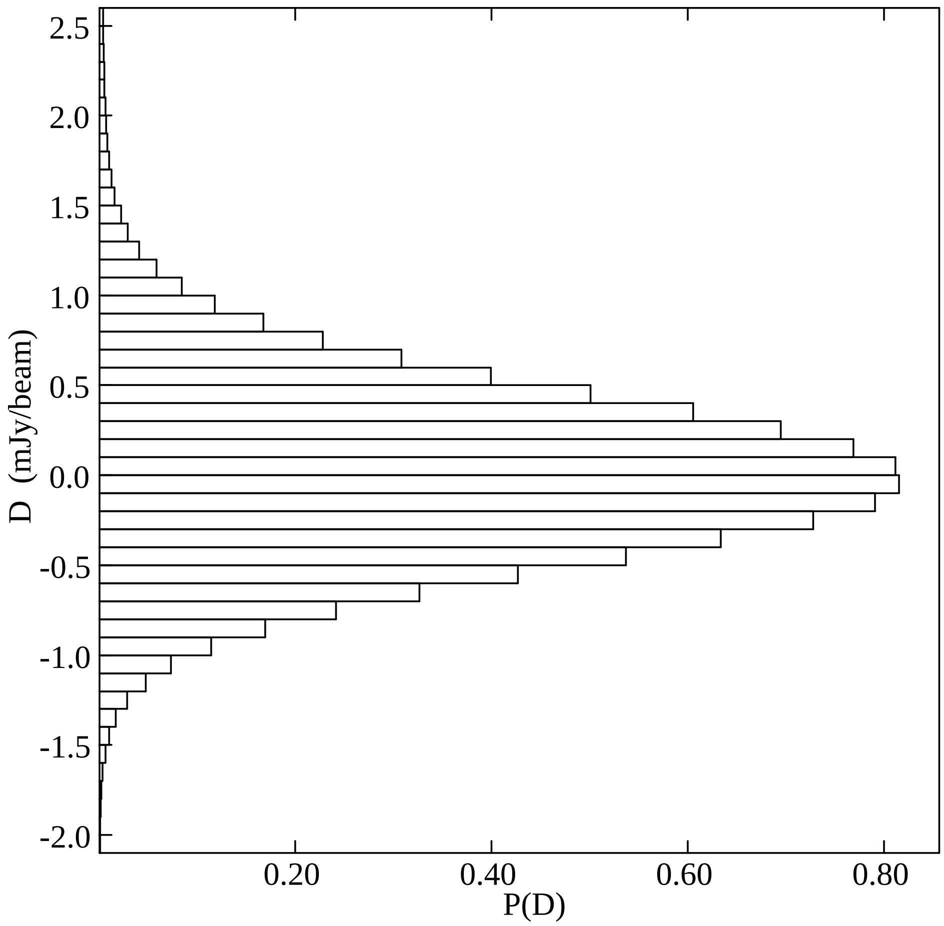

Fig. 26.— Brightness "deflection" distribution of the NVSS image J2230+84. Abscissa: probability (mJy beam^{-1})$^{-1}$. Ordinate: brightness (mJy beam^{-1})

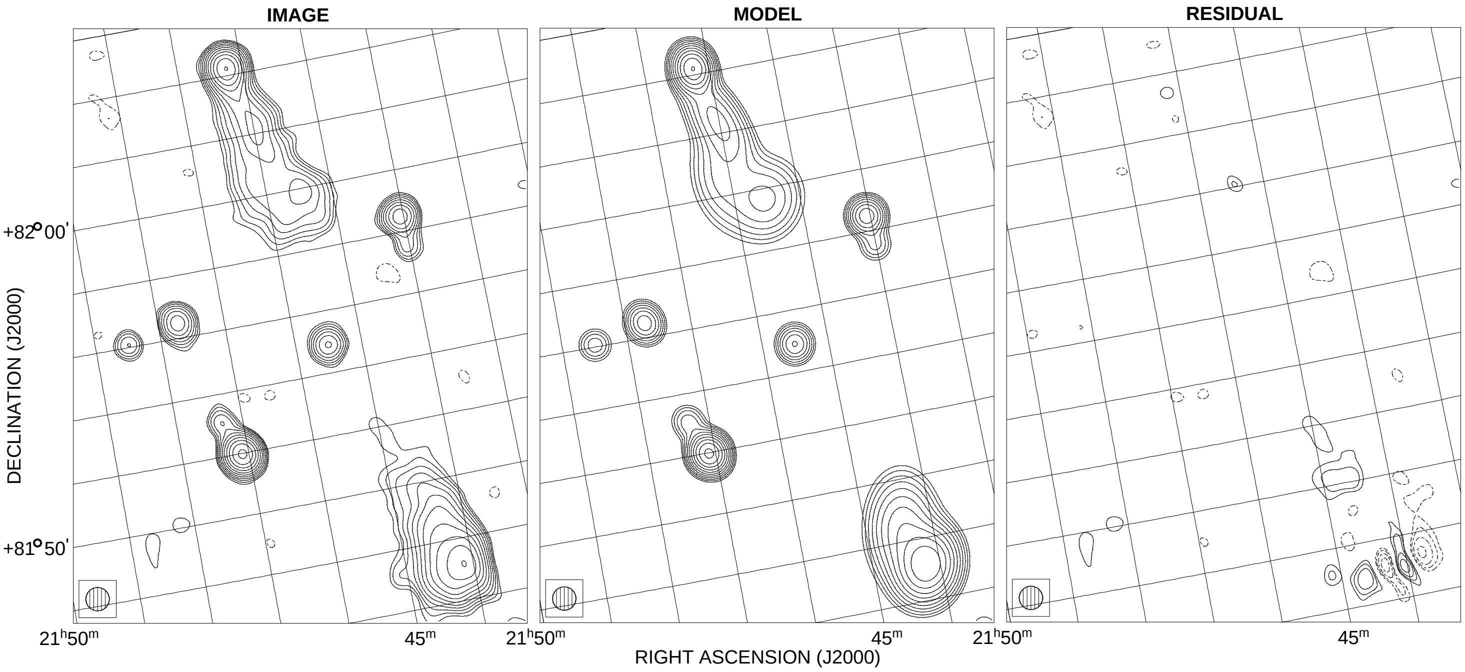

Fig. 27.— Even extended sources on the NVSS images (left panel) can usually be approximated by a small number of elliptical Gaussians (center panel). The difference between the image and the model (right panel) is small except near strong, complex sources. Contours: 1 mJy beam$^{-1} \times \pm 2^0, \pm 2^{1/2}, \pm 2^1, \pm 2^{3/2} \ldots$ Abscissae: J2000 right ascension. Ordinates: J2000 declination.

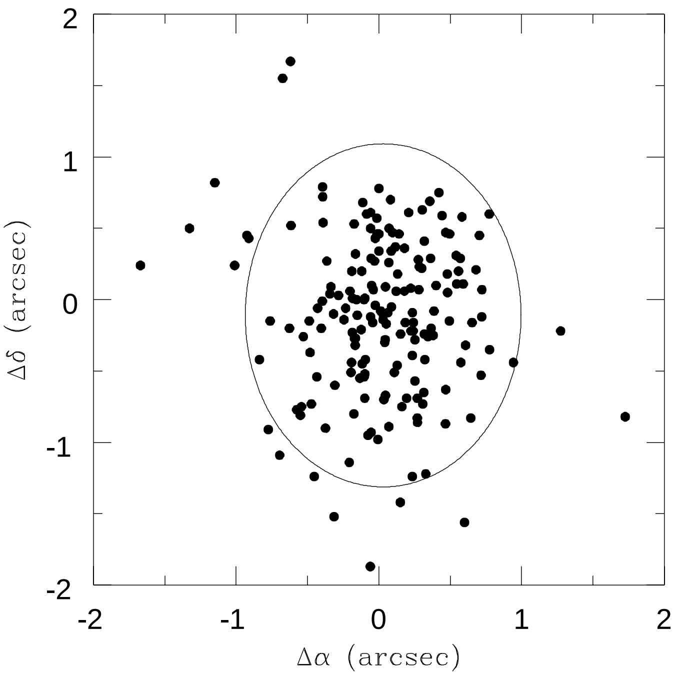

Fig. 28.— NVSS image position errors for strong point sources. The semi-axes of the 90% confidence ellipse shown are $(2\ln 10)^{1/2}$ times the rms errors $\epsilon_\alpha = 0\farcs45$, $\epsilon_\delta = 0\farcs56$. The mean image offsets are $\langle\Delta\alpha\rangle = +0\farcs025 \pm 0\farcs022$ and $\langle\Delta\delta\rangle = -0\farcs113 \pm 0\farcs027$. Abscissa: right ascension error (arcsec). Ordinate: declination error (arcsec).

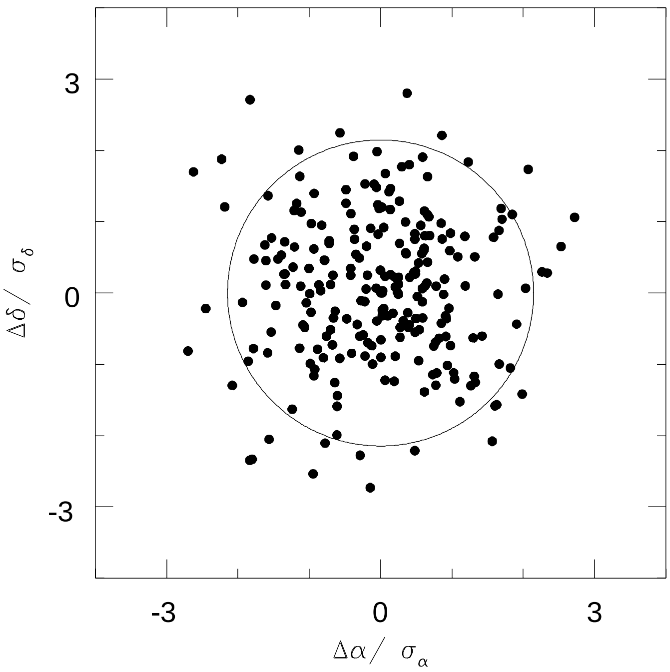

Fig. 29.— NVSS position errors for weak sources, in units of the calculated rms position uncertainties σ_α, σ_δ, along with the 90% confidence error circle. Abscissa: normalized right ascension error. Ordinate: normalized declination error.

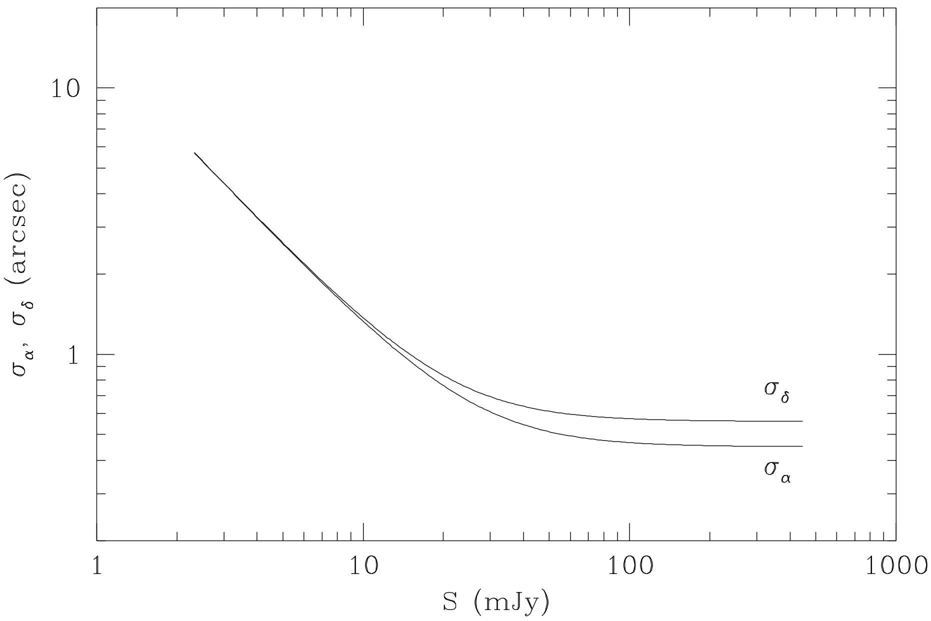

Fig. 30.— The typical rms position uncertainty (σ_α or σ_δ) for a point source of flux-density S in the NVSS catalog. Abscissa: flux density (mJy). Ordinate: rms position error (arcsec).

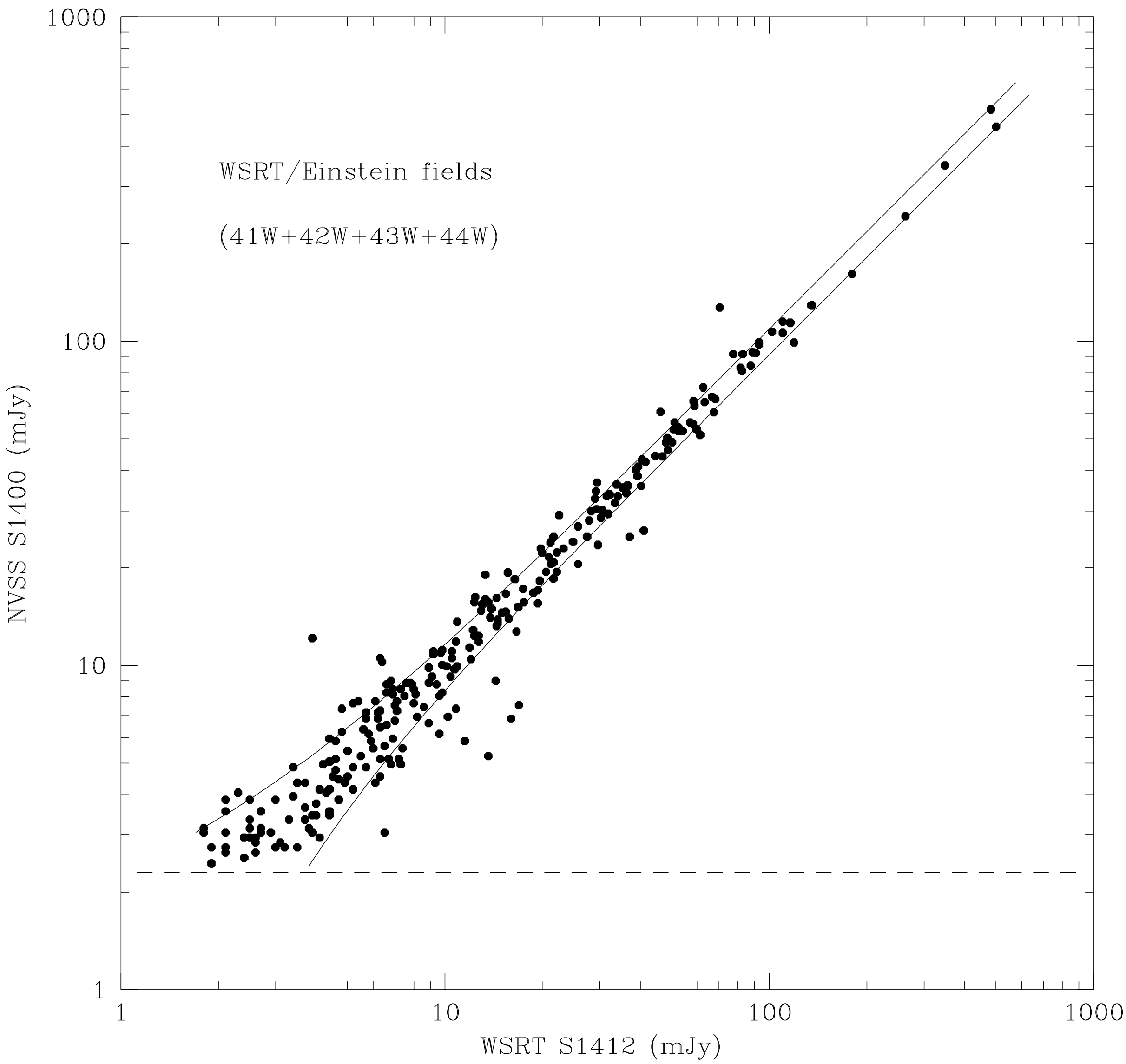

Fig. 31.— Flux-flux diagram comparing the NVSS flux densities with WSRT/Einstein flux densities. The NVSS catalog cutoff is indicated by the broken line. The solid curves are the 90% confidence limits. Abscissa: WSRT 1412 MHz flux density (mJy). Ordinate: NVSS 1400 MHz flux density (mJy).

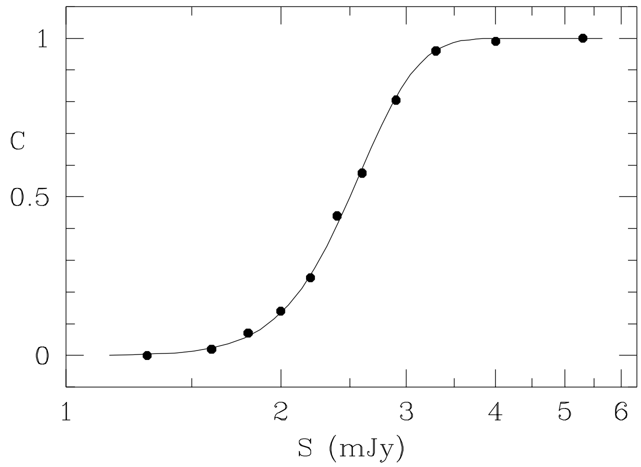

Fig. 32.— Simulations (filled circles) with artificial point sources indicate that the incremental completeness of the NVSS catalog is 50% at $S = 2.5$ mJy. The variation of incremental completeness with flux density is consistent with the integral of a Gaussian error distribution whose standard deviation is 0.45 mJy (curve), the rms noise and confusion error for a point source. Abscissa: True source flux density (mJy). Ordinate: Incremental completeness (dimensionless).